J. Fluid Mech. (2000), *vol.* 413, *pp.* 247–285. Printed in the United Kingdom

© 2000 Cambridge University Press

Acoustically generated vorticity in an internal flow

By Q. ZHAO[1], P. L. STAAB[2], D. R. KASSOY[3] AND K. KIRKKOPRU[4]

[1]AU100, Hewlett-Packard Company, 815 14th Street S. W., Loveland, CO 80537, USA

[2]Department of Applied Mathematics, University of Colorado, CB 526, Boulder CO 80309-0526, USA

[3]Department of Mechanical Engineering, University of Colorado, CB 051, Boulder CO 80309-0051, USA

[4]Mechanical Engineering Department, Istanbul Technical University, Gumussuyu-Taksim 80191 Istanbul, Turkey

(Received 8 March 1997 and in revised form 3 February 2000)

A mathematical model is formulated to describe the initiation and evolution of intense unsteady vorticity in a low Mach number (M), weakly viscous internal flow sustained by mass addition through the sidewall of a long, narrow cylinder. An $O(M)$ axial acoustic velocity disturbance, generated by a prescribed harmonic transient endwall velocity, interacts with the basically inviscid rotational steady injected flow to generate time-dependent vorticity at the sidewall. The steady radial velocity component convects the vorticity into the flow. The axial velocity associated with the vorticity field varies across the cylinder radius and in particular has an instantaneous oscillatory spatial distribution with a characteristic wavelength $O(M)$ smaller than the radius. Weak viscous effects cause the vorticity to diffuse on the small radial length scale as it is convected from the wall toward the axis. The magnitude of the transient vorticity field is larger by $O(M^{-1})$ than that in the steady flow.

An initial-boundary-value formulation is employed to find nonlinear unsteady solutions when a pressure node exists at the downstream exit of the cylinder. The complete velocity consists of a superposition of the steady flow, an acoustic (irrotational) field and the rotational component, all of the same magnitude.

1. Introduction

Intense transient vorticity can be generated in a tubular internal flow by an interaction between a forced acoustic field and fluid injected normally from the cylinder sidewall. This occurs at a given axial location because the transient axial gradient of the acoustic pressure drives time-dependent wall shear stress variations. The resulting radial gradient of the axial velocity is convected into the cylinder by the injected flow field. As a result, one finds co-existing irrotational and rotational disturbances of the same magnitude.

The spatial distribution and time-history of the vorticity depend upon the characteristic amplitude of the wall injection speed (V'_{r0}), the length (L') and radius (R') of the cylinder, the frequency of the acoustic forcing (ω'), and the fluid properties. It follows that the crucial non-dimensional parameters include, the flow Reynolds

https://doi.org/10.1017/S0022112000008454 Published online by Cambridge University Press

(Re) and Mach (M) numbers along with the aspect ratio (δ) and a frequency (ω), all defined below.

The intense transient vorticity is confined to a viscous acoustic boundary layer, small in transverse dimension with respect to the cylinder radius, when the wall injection speed is sufficiently small. As the injection rate increases, the boundary layer thickness grows and the importance of viscous forces is reduced, relative to the axial pressure gradient effect. Eventually, the boundary layer concept is invalid, the flow is only weakly viscous and transient vorticity is present throughout the cylinder. One objective of the present work is to describe a mathematical formulation based on perturbation methods, valid for wall injection rates sufficiently large to preclude the viability of the viscous acoustic boundary layer model. Solutions to the model describe the time-history of the co-existing acoustic and rotational flow fields.

Flandro (1974) provides an early assessment of the importance of vorticity in an acoustic boundary layer. He studies the impact of a small axial pressure gradient, varying harmonically in time, on the viscous processes occuring adjacent to a surface from which a steady, spatially uniform transverse injection occurs. A linear equation for axial velocity contains a balance of convection, pressure gradient forces and viscous diffusion. The solution describes a shear wave convecting away from the wall, with an amplitude that is damped by viscous effects. One finds intense, transient vorticity in the boundary layer, relative to the weaker steady vorticity associated with the inviscid, rotational Culick (1966) solution valid beyond the boundary layer. The solution is valid only for small injection Mach number $M_b = O(R_A^{-1/2})$ where $R_A \gg 1$ is the appropriate acoustic Reynolds number for the chamber. Related work has been described by Tien (1972) and Flandro (1986).

Important extensions of Flandro's concepts have been developed by Zinn and coworkers (Chen, Hegde & Zinn 1990; Hegde, Chen & Zinn 1986; Hegde & Zinn 1986; Matta & Zinn 1993) in the context of acoustic boundary layers that are thin relative to the transverse dimension of the internal flow. These research efforts are motivated by the need to understand how energy is transferred from the axial acoustic field to the fluid injected from the sidewall as the latter is turned toward the axial flow direction from its initially transverse motion (flow turning). Hegde *et al.* (1986) recognized explicitly that for sufficiently large injection rates, '... the boundary layer may encompass a significant portion of the duct...' and that in this case '... viscous effects must then be included in the analysis of the (entire chamber)'. However, there was no specific modelling of this particular situation.

The pervasive presence of rotational disturbances throughout an injected internal flow was first demonstrated in the experiments of Brown and co-workers (Brown *et al.* 1986*a*, *b*; Brown & Shaeffer 1992). They injected gas through the porous sidewall of a cylinder/nozzle configuration. A periodic mass injection technique is used to induce single-frequency disturbances into the system. Hot-wire measurements of the time-averaged axial velocity field at numerous axial and radial locations are used to show that large, local radial gradients of the time-averaged axial velocity are present across the entire cylinder cross-section, with a characteristic length scale far smaller than the radius. The associated radial spatial oscillations in the axial speed are not compatible with profiles predicted by a traditional acoustic analysis (Culick & Yang 1992), although associated pressure variations appear to be purely acoustic in character. The experimental observations suggest the need for a mathematical model of the disturbed, sidewall-injected flow system that can deal with co-existing acoustic and rotational flow processes throughout the chamber geometry, as well as resolve

https://doi.org/10.1017/S0022112000008454 Published online by Cambridge University Press

transverse flow processes on radial length scales short with respect to the overall transverse dimension of the chamber geometry.

Vuillot & Avalon (1991) and Vuillot (1995) have repeatedly emphasized the importance of vorticity in these injected internal unsteady flows. They point out that the assumptions built into the acoustic stability theory reviewed extensively by Culick & Yang (1992) have the effect of '... cancelling all trace of vorticity of the flows'. In particular, the velocity perturbation is proportional to the gradient of the pressure perturbation. Clearly, an irrotational formulation cannot account for the highly rotational, unsteady flow field observed in experiments, and seen in the computational results described below.

Casalis, Avalon & Pineau (1998) and Avalon, Casalis & Grifford (1998) have included rotational disturbances in a purely hydrodynamic stability study of planar flow in a channel with steady sidewall injection. Non-parallel stability theory is used to do a linear analysis of the steady solution (see Taylor 1956). Results are sensitive to the transverse velocity component of the steady flow, neglected in many traditional studies of acoustic stability (see Culick & Yang 1992) and demonstrate the importance of non-parallel affects.

Flandro & Roach (1992) describe an initial attempt at developing an analytically based model of the Brown and co-worker experiments. A more complete version is given in Flandro (1995*a*) where a theory is developed for co-existing transient vorticity and acoustic waves throughout a cylindrical chamber. The steady, inviscid rotational Culick (1966) solution, associated with a uniform injection Mach number $M_b \ll 1$, is disturbed by a smaller $O(\epsilon)$ acoustic velocity that varies harmonically in time. Perturbation methods valid for $M_b \to 0$ and a linear stability approach are used to derive an inviscid, linear, small-disturbance equation for the rotational part of the axial velocity, which is assumed to have quasi-steady time dependence.

The solution satisfies the no-slip condition on the sidewall, and symmetry conditions on the axis. The equation itself can be used to show that the amplitude of the vorticity generated at the sidewall surface is $O(\epsilon/M_b^2)$ relative to the vorticity associated with the steady Culick profiles. Hence for sufficiently large values of ϵ the transient vorticity can be more intense than is the steady field vorticity. The rotational axial velocity solution is characterized by shear waves of small radial length scale that are convected into the cylinder by the steady Culick velocity components. The time-averaged axial velocity variation with radius is qualitatively similar to the spatial oscillations observed experimentally by Brown *et al.* (1986*a*, *b*) and Brown & Shaeffer (1992).

Flandro (1995*a*) notes that viscous effects will have a minor impact on the inviscid rotational solution for the vorticity distribution, using an argument based on his earlier viscous acoustic boundary layer theory, Flandro (1974). That work is valid mathematically only adjacent to the injection surface because the transverse speed is assumed to be constant. Hence it appears unlikely that the results can be applied to the entire cylinder, where the radial speed must vanish at the centreline.

A more systematic effort is made to consider the impact of viscosity in Flandro (1995*b*), in the context of small-disturbance linear stability theory. As in the previous paper the asymptotic methods, valid for $M_b \to 0$, are applied in an intuitive manner. It is not always apparent why terms in equations are included or neglected. The results of the linear analysis suggest that viscous effects are most important near the centreline of the cylinder, a result quite different from conclusions of the present work.

Majdalani & Van Moorhem (1997) also describe a small-disturbance linear stability

https://doi.org/10.1017/S0022112000008454 Published online by Cambridge University Press

theory that includes the impact of viscosity on the vorticity distribution. Their formulation is based on a limit of large acoustic Reynolds number with the injection Mach number M_b fixed. Solutions are assumed to have quasi-steady time dependence. The results can be interpreted to mean that vorticity is weak but pervasive throughout the cylindrical flow.

More recently, Majdalani, Flandro & Roh (1998) and Majdalani (1998) have compared the earlier results of Flandro (1995*a*) and Majdalani & Van Moorhem (1997) based on two different asymptotic methodologies with numerical solutions. Both studies of analytical solutions compare favourably with these to the full Navier–Stokes equation. These results, once again, confirm that a complete understanding of the linear instability process in an unsteady injected internal flow requires that the full transverse velocity field is retained in the mathematical model.

Significant efforts have been made to develop multidimensional computational models for wall-injected internal flow including the resolution of the identifiable layers containing rotational flow. Baum & Levine (1987) used the Navier–Stokes equations to evaluate the internal flow response to imposed disturbances. Baum (1989, 1990) has used the Reynolds-averaged compressible Navier–Stokes equations, including a k–ϵ model, to find initial value solutions for the transient flow in a cylindrical geometry. Sidewall injection is steady and uniform and disturbances are created by a prescribed harmonic variation of the axial speed on the endwall (piston effect). Results are obtained for $R_A = 3 \times 10^7$ and $M_b = 2.2 \times 10^{-3}$. Acoustic boundary layers adjacent to the injecting surface, containing significant radial gradients of the axial velocity, appear to be quite thin, usually confined to a few percent of the cylinder radius. In one case vorticity is seen as far as about 20% of the radius from the sidewall. These results are quite different from the experimental observations of Brown and co-workers which appear to include co-existing vorticity and acoustic waves across the entire cylinder. The difference likely rises from (*a*) the distribution of grid points across the cylinder (most are packed close to the sidewall in anticipation of traditional acoustic boundary layer behaviour), and (*b*) short run times (not enough time has elapsed after the introduction of the disturbance to convect the vorticity generated at the sidewall very far out into the cylinder). The former implies that the computation can resolve the short length scale radial gradients only in the vicinity of the sidewall. Even if the vorticity convects beyond the region with sufficient grid resolution, its presence cannot be discriminated by the larger grids in the central portion of the cylinder.

Vuillot & Avalon (1991) use laminar Navier–Stokes equations to develop an initial value study of flow in a planar rectangular chamber where a prescribed harmonic disturbance in pressure is applied on the exit plane. The calculation is carried out for $R_A = 3 \times 10^4$ and $M_b = 0.0098$, corresponding to a relatively viscous system. Here again the transverse gridding is packed near the wall, although a finer resolution is present further out into the field than in the Baum work. The computation times are long enough for the vorticity generated at the wall to reach the centreline. Significant transverse gradients in the axial velocity (vorticity) are found out to about 50% of the half-height of the rectangle.

Smith, Roach & Flandro (1993) also find vorticity present in a large portion of a cylindrical geometry. Their computation is done to simulate the experiments of Brown *et al.* (1986*a*, *b*) and Brown & Shaeffer (1992). Significant radial gradients in the axial velocity are seen about halfway out toward the centreline. Here again, the run times are sufficiently long to move the vorticity well away from the injection surface, and the gridding distribution enables it to be resolved, at least part way out

https://doi.org/10.1017/S0022112000008454 Published online by Cambridge University Press

into the cylinder. The authors suggest that the spatial resolution may not be adequate further out.

Acoustic processes in a thermally active internal flow with combustion have been studied computationally by Tseng *et al.* (1994), based on the use of the compressible Navier–Stokes equations. Steady, spatially uniform injection of a propane–air mixture occurs at the porous sidewall of a planar, rectangular geometry. A small (2%) time-dependent harmonic pressure disturbance is applied at either the head end (travelling wave solutions) or the exit plane (standing wave solutions) of the chamber. Vorticity, as represented by large transverse gradients in the axial velocity, is found in a thin layer near the injecting surface, on the order of 10–15% of the channel half-height. This confinement of the rotational flow distribution is due in part to short run times and in part to a coarse grid distribution in the central portion of the rectangle. It is important to note that flame resolution requires a significant number of points near the injection surface, and not surprisingly the vorticity is seen most strongly in this highly resolved region.

Roh & Yang (1995) have done a similar computation for combustion processes associated with double base propellants. Longer run times and better spatial resolution leads to the appearance of vorticity through 75% of the half-height of the rectangular height.

The modelling in the present paper is described in terms of a quasi-analytical asymptotic analysis of an initial-boundary value problem with imposed boundary disturbances of significant magnitude. In contrast to the previously cited small-disturbance linear-stability-based theories with quasi-steady time dependence, we study an evolving fully transient flow including the complete acoustic field compatible with the cylindrical geometry and imposed boundary conditions.

Our work focuses on the fluid dynamics occurring in a finite length (L') cylinder of radius R' with one open end. Steady radial mass addition from the sidewall creates a primarily inviscid rotational internal flow which is affected weakly by viscosity (Taylor 1956; Culick 1966). The characteristic axial flow Reynolds number, and the axial flow Mach number are large and small respectively. The 'large' or 'massive' injection velocity needed to diminish the significance of viscosity near the sidewall has been considered in the context of injected boundary layer theory by Cole & Aroestry (1968).

Imposed time-dependent axial velocity disturbances on the closed end add transient energy to the internal flow and generate an acoustic field present throughout the cylinder. The characteristic magnitude of the imposed disturbance is chosen to be the same as that of the steady injection-induced axial velocity in order to study a relatively large transient response of the system. Axial acoustic waves interact with injected fluid particles to create intense transient axially distributed vorticity on the sidewall, far larger than that of the primarily inviscid steady rotational flow produced by the sidewall injection alone. The vorticity is convected into the cylinder along pathlines associated with the internal flow.

The transient vorticity is confined to a weakly viscous 'transition layer' adjacent to the wall for sufficiently small values of the wall injection speed. This layer thickness is large compared to a viscous acoustic layer, but smaller than the cylinder radius. The convected vorticity is diffused on a transverse scale that is small compared to the transition layer dimension. However, over the latter scale, the accumulated impact of weak diffusion damps out the intense transient vorticity. Beyond the transition layer one finds a 'core' flow consisting of the irrotational acoustic field and the less intense steady vorticity.

https://doi.org/10.1017/S0022112000008454 Published online by Cambridge University Press

Transient vorticity is present throughout the cylinder when the wall injection speed is sufficiently large, as defined explicitly by the model. In this case the transient flow field is weakly viscous across the entire cylinder. Again, vorticity is diffused on a short length scale, but the accumulated viscous damping is not sufficient to prevent the eventual appearance of vorticity at all radial locations except on the axis, where symmetry requires a zero vorticity value.

The mathematical model is formulated in terms of an initial value problem with explicit time-dependent forcing conditions on the closed end of the cylinder. A multiple-scale approach is used to describe co-existing phenomena (steady, inviscid rotational flow field; planar, irrotational acoustic wave field; transient, weakly viscous rotational flow field) evolving simultaneously on two disparate transverse dimensions.

Solutions for the transition layer/core model are given in analytical terms, based on asymptotic expansions in the small axial flow Mach number (M). The planar acoustic pressure and axial velocity solutions are eigenfunction expansions appropriate to the geometry and prescribed boundary conditions. Both non-resonant and resonant cases are included. The axial speed in the transition layer depends upon two transverse variables of disparate size. A small scale variable is used to describe relative short-wavelength spatial oscillations embedded within the transition layer. The amplitude of the oscillations, dependent on the larger scale variable, vanishes exponentially fast as the transition layer edge is approached. Asymptotic properties of the solution are used to define the parameter conditions for which the transition layer/core concept fails, and for which vorticity can be present across the entire cylinder.

A multiple scale approach is used to formulate the model for the co-existing acoustic and rotational flow fields that evolve simultaneously in the cylinder when vorticity may be present at all radial locations. Planar acoustic solutions, composed of a forced mode and eigenmodes, are derived from a linear wave equation driven by a forced endwall boundary condition. The lowest-order rotational part of the axial speed field is described by an inviscid linear first-order wave equation. This implies that vorticity generated at the sidewall by an axial pressur gradient/injected fluid interaction is convected toward the cylinder axis by the radial component of the injected flow field. For sufficiently small times a sharp front separates the intense transient vorticity initiated at the wall from the much weaker steady vorticity of the Culick (1966) solution. Eventually, the front location asymptotes to the cylinder axis and vorticity is present everywhere.

Although the lowest-order vorticity transport process is described by an inviscid equation, a higher-order analysis is used to prove that weak viscous and nonlinear effects are pervasive in the flow field for useful values of the significant parameters, including the relatively large boundary disturbance considered here. In particular, vorticity is diffused by viscosity on a length scale short compared with the cylinder radius. The complete initial-value solution for the rotational part of the axial speed is derived from a nonlinear diffusion equation using direct numerical computations. Results are given for several parameter values at various locations in the cylinder and describe how the energy input at the endwall is partitioned between the acoustic and rotational components of the flow field.

Evaluation and interpretation of the results show that a complex vorticity distribution is present throughout the cylinder sufficiently long after the disturbance is initiated at the endwall. In part the spatial variations result from the inclusion of numerous Fourier modes in the acoustic solutions that are responsible for the appearance of the vorticity. Fully computational methods are used by Kirkkopru, Kassoy

https://doi.org/10.1017/S0022112000008454 Published online by Cambridge University Press

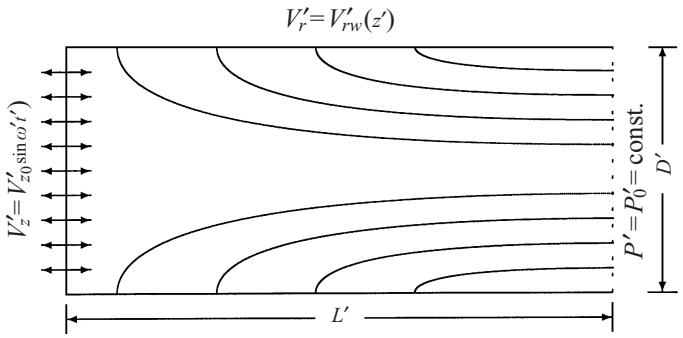


FIGURE 1. The cylindrical rocket engine chamber model of length L', diameter D', a left closed end and a right open end with pressure condition $P' = P_0' = \text{const}$. The left end has a condition that $V_z = A \sin \omega t$ where ω' is on the order of the first few axial acoustic modes. The curves within the chamber indicate example pathlines at a particular time.

& Zhao (1995, 1996) and Kirkkopru *et al.* (1999) to provide supporting evidence for the solutions found here by quasi-analytical means.

2. Mathematical formulation

An internal flow arising from time-invariant sidewall mass addition in a cylindrical tube of length L' and diameter D' is shown schematically in figure 1. The oscillatory endwall disturbance in the axial speed V_z' is the source of acoustic waves in the cylinder. A pressure node boundary condition is assumed at the downstream end of the tube.

The complete non-dimensional equations describing the fluid dynamics and acoustics for an axisymmetric system can be written in the form

$$0 = \frac{\partial \rho}{\partial t} + M\left(\frac{1}{r}\frac{\partial}{\partial r}(\rho r V_r) + \frac{\partial}{\partial z}(\rho V_z)\right), \tag{2.1}$$

$$\rho \frac{\mathrm{D}V_r}{\mathrm{D}t} = -\delta^2 \frac{1}{\gamma M}\frac{\partial P}{\partial r} + \delta^2 \frac{M}{Re}\left\{\frac{\partial}{\partial z}\mu\left[\frac{1}{\delta^2}\frac{\partial V_r}{\partial z} + \frac{\partial V_z}{\partial r}\right] + 2\frac{\partial}{\partial r}\mu\left[\frac{\partial V_r}{\partial r} - \frac{1}{3}\left(\frac{1}{r}\frac{\partial (rV_r)}{\partial r} + \frac{\partial V_z}{\partial z}\right)\right] + \frac{2\mu}{r}\left[\frac{\partial V_r}{\partial r} - \frac{V_r}{r}\right]\right\}, \tag{2.2}$$

$$\rho \frac{\mathrm{D}V_z}{\mathrm{D}t} = -\frac{1}{\gamma M}\frac{\partial P}{\partial z} + \delta^2 \frac{M}{Re}\left\{\frac{\mu}{r}\left[\frac{1}{\delta^2}\frac{\partial V_r}{\partial z} + \frac{\partial V_z}{\partial r}\right] + \frac{\partial}{\partial r}\mu\left[\frac{1}{\delta^2}\frac{\partial V_r}{\partial z} + \frac{\partial V_z}{\partial r}\right]\right\} + 2\frac{M}{Re}\frac{\partial}{\partial z}\mu\left[\frac{\partial V_z}{\partial z} - \frac{1}{3}\left(\frac{1}{r}\frac{\partial (rV_r)}{\partial r} + \frac{\partial V_z}{\partial z}\right)\right], \tag{2.3}$$

$$\rho C_v \frac{\mathrm{D}T}{\mathrm{D}t} = -(\gamma - 1)MP\left[\frac{1}{r}\frac{\partial (rV_r)}{\partial r} + \frac{\partial V_z}{\partial z}\right] + \frac{\delta^2 M}{Re}\frac{\gamma}{Pr}\left[\frac{1}{\delta^2}\frac{\partial}{\partial z}\left(k\frac{\partial T}{\partial z}\right) + \frac{1}{r}\frac{\partial}{\partial r}\left(kr\frac{\partial T}{\partial r}\right)\right] + \frac{M^3\delta^2}{Re}\Phi, \tag{2.4}$$

$$P = \rho T \tag{2.5}$$

https://doi.org/10.1017/S0022112000008454 Published online by Cambridge University Press

where

$$\frac{\mathrm{D}}{\mathrm{D}t} = \frac{\partial}{\partial t} + M\left(V_r\frac{\partial}{\partial r} + V_z\frac{\partial}{\partial z}\right),$$

and Φ is the viscous dissipation function. The non-dimensional variables are defined in terms of dimensional quantities (with a prime) by

$$\left.\begin{aligned} &\rho = \frac{\rho'}{\rho_0'}, \quad P = \frac{P'}{P_0'}, \quad T = \frac{T'}{T_0'}, \quad V_r = \frac{V_r'}{V_{r0}'}, \quad V_z = \frac{V_z'}{V_{z0}'}, \\ &z = \frac{z'}{L'}, \quad r = \frac{r'}{R'}, \quad t = \frac{t'}{t_a'}, \quad k = \frac{k'}{k_0'}, \quad \mu = \frac{\mu'}{\mu_0'}, \quad C_v = \frac{C_v'}{C_{v0}'}. \end{aligned}\right\} \tag{2.6}$$

The reference value P_0' is the initial static pressure in the cylinder, while the analogous density and temperature values ρ_0', T_0' respectively represent properties of the injected fluid. The known characteristic injection speed V_{r0}' is related to the derived characteristic axial speed V_{z0}' by the approximate mass conservation relationship $V_{z0}' = \delta V_{r0}'$. Here, the large aspect ratio $\delta = L'/R' \gg 1$ and R' is the tube radius. Characteristic length scales for the axial and radial variables are defined by L' and R' respectively. Time is non-dimensionalized with respect to the axial acoustic time $t_a' = L'/C_0'$, where $C_0' = (\gamma \mathscr{R}' T_0')^{1/2}$ is the characteristic sound speed and $\mathscr{R}'$ is the gas constant. The reference material properties k_0', μ_0' and C_{v0}' are defined at temperature T_0'. The parameter γ is the ratio of specific heats and

$$Re = \frac{\rho_0' V_{z0}' L'}{\mu_0'}, \quad Pr = \frac{\mu_0' C_{p0}'}{k_0'}, \quad M = \frac{V_{z0}'}{C_0'}, \tag{2.7}$$

where typically the Prandtl number $Pr = O(1)$, the axial Mach number $M \ll 1$ and the axial flow Reynolds number $Re \gg 1$. It is noted that the Reynolds number used here is $O(M)$ smaller than the acoustic Reynolds number.

Initially, a steady flow exists in the cylinder, driven by spatially distributed normal injection from the wall where the no-slip condition is satisfied. Symmetry prevails along the axis. The mathematical form of the steady flow boundary conditions may be written as

$$r = 0: \quad V_r = \frac{\partial V_z}{\partial r} = 0, \tag{2.8}$$

$$r = 1: \quad V_r = -V_{rw}(z), \; V_z = 0, \; T = 1, \tag{2.9}$$

$$z = 0: \quad V_z = 0, \tag{2.10}$$

$$z = 1: \quad P = 1. \tag{2.11}$$

The steady flow is disturbed at $z = 0$ by imposing a harmonic endwall axial velocity variation that is independent of the radial coordinate,

$$z = 0: \quad V_z = A\sin\omega t; \quad t \geqslant 0: \quad 0 \leqslant r \leqslant 1, \tag{2.12}$$

where the amplitude $A = O(1)$.

It should be noted that the imposed endwall disturbance, of the same order of magnitude as that of the steady axial speed, is the source of mechanical and thermodynamical disturbances of like magnitude in the gas. These relatively large variations are described by a weakly nonlinear theory that differs from the small-disturbance theory used by Flandro (1995*b*).

The sidewall injection is strong in the sense that $V_{r0}' \gg V_{z0}'/Re^{1/2}$ (see Cole &

https://doi.org/10.1017/S0022112000008454 Published online by Cambridge University Press

Aroesty 1968), which implies that the parameter combination seen in (2.2) and (2.3), $\delta^2/Re \ll 1$. The hard blowing condition implies that the flow is basically inviscid, even near the injecting surface, so that no acoustic boundary layer is expected.

3. Steady-state flow

The steady-state flow generated by time-independent mass addition on the sidewall can be described in terms of the asymptotic expansions:

$$(P, \rho, T) \sim 1 + M^2(P_{0s}, \rho_{0s}, T_{0s}) + o(M^2), \qquad (V_z, V_r) \sim (V_{z0s}, V_{r0s}) + o(1), \tag{3.1}$$

valid in the limit $M \to 0$. The expansion in (3.1) can be used in (2.1)–(2.5) to find the leading-order equations

$$\frac{1}{r}\frac{\partial(rV_{r0s})}{\partial r} + \frac{\partial V_{z0s}}{\partial z} = 0, \tag{3.2}$$

$$P_{0s} = P_{0s}(z), \tag{3.3}$$

$$V_{r0s}\frac{\partial V_{z0s}}{\partial r} + V_{z0s}\frac{\partial V_{z0s}}{\partial z} = -\frac{1}{\gamma}\frac{\partial P_{0s}}{\partial z}. \tag{3.4}$$

These describe an incompressible, inviscid, rotational flow that satifies the no-slip and injection boundary conditions on the sidewall and symmetry conditions on the axis, given in (2.8)–(2.11). The transport terms are excluded from the leading-order equations because $\delta^2/Re \ll 1$. Equation (3.3) arises because the aspect ratio $\delta \gg 1$. Solutions for the radial and axial velocity, as well as the pressure distribution can be written in the form

$$V_{r0s} = -\frac{V_{rw}(z)}{r}\sin(\tfrac{1}{2}\pi r^2), \tag{3.5}$$

$$V_{z0s} = \left(\pi\int_0^z V_{rw}(\tau)\mathrm{d}\tau\right)\cos(\tfrac{1}{2}\pi r^2), \tag{3.6}$$

$$P_{0s} = \gamma\pi^2\int_z^1\left[V_{rw}(\hat{z})\int_0^{\hat{z}} V_{rw}(\tau)\mathrm{d}\tau\right]\mathrm{d}\hat{z}, \tag{3.7}$$

where $-V_{rw}(z) > 0$ is an arbitary time-independent sidewall injection distribution. Related solutions can be found in Culick (1966) and Taylor (1956). It should be noted that Balakrishnan, Liñán & Williams (1991) obtained a fully compressible solution valid for $M = O(1) < 1$.

4. Core/transition layer solutions

The viscous acoustic boundary layer theory of Flandro (1974) describes intense transient vorticity generation and evolution in a layer of non-dimensional thickness $O(R_A^{-1/2})$ where the acoustic Reynolds number $R_A \equiv Re/M \gg 1$. The solution is valid formally for a small injection Mach number $M_b = O(R_A^{-1/2})$.

It is of interest to develop a theory for larger injection rates, when the transverse dimension of the layer containing vorticity remains smaller than the radius of the cylinder, but is larger than that permitted by the model of Flandro (1974). The conceptual approach focuses first on a central 'core' region containing the weak vorticity of the steady solutions in (3.5)–(3.7) and irrotational linear acoustic disturbances of the same magnitude, driven by the prescribed endwall disturbances in (2.12). The thinner transition layer contains the intense transient vorticity. A multiple-length-scale

https://doi.org/10.1017/S0022112000008454 Published online by Cambridge University Press

asymptotic analysis, used to develop the solutions, describes how weak but pervasive viscosity affects the flow physics in the transition layer.

The asymptotic expansions for the unsteady core flow can be written as

$$(P,\rho,T)\sim 1+\sum_{n=0} M^{n+1}(\widetilde{P}_n,\widetilde{\rho}_n,\widetilde{T}_n),\quad (V_r,V_z)\sim (V_{r0s},V_{z0s})+\sum_{n=0} M^{n}(\widetilde{V}_{rn},\widetilde{V}_{zn}) \tag{4.1}$$

in the limit $M\to 0$. Equation (4.1) can be used in (2.1)–(2.5) to derive the lowest-order equations, valid in the limit $M\to 0$, with $\delta^2/Re\to 0$,

$$\frac{\partial\widetilde{\rho}_0}{\partial t}+\frac{1}{r}\frac{\partial(r\widetilde{V}_{r0})}{\partial r}+\frac{\partial\widetilde{V}_{z0}}{\partial z}=0, \tag{4.2}$$

$$\frac{\partial\widetilde{V}_{z0}}{\partial t}=-\frac{1}{\gamma}\frac{\partial\widetilde{P}_0}{\partial z} \tag{4.3}$$

$$\frac{\partial\widetilde{T}_0}{\partial t}=(\gamma-1)\frac{\partial\widetilde{\rho}_0}{\partial t}, \tag{4.4}$$

$$\widetilde{\rho}_0=\widetilde{P}_0+\widetilde{T}_0. \tag{4.5}$$

The velocity components in (4.2) are composed of both a steady state and a transient part of the same magnitude: $(V_{z0},V_{r0})=(V_{z0s},V_{r0s})+(\widetilde{V}_{z0},\widetilde{V}_{r0})$. Subtraction of the steady-state equations (3.2)–(3.4) from (4.2)–(4.5) provides the transient acoustic mathematical problem. The boundary condition in (2.12), which is independent of the radial variable, implies that the radial speed, $\widetilde{V}_{r0}=0$.

4.1. *The planar acoustic solution in the core*

The transient part of the leading-order equations can be combined into a planar wave equation for the axial velocity component:

$$\frac{\partial^2\widetilde{V}_{z0}}{\partial t^2}=\frac{\partial^2\widetilde{V}_{z0}}{\partial z^2} \tag{4.6}$$

subject to the initial and boundary conditions

$$t=0:\quad \widetilde{V}_{z0}=0,\quad \frac{\partial\widetilde{V}_{z0}}{\partial t}=0, \tag{4.7}$$

$$z=0:\quad \widetilde{V}_{z0}=A\sin\omega t, \tag{4.8}$$

$$z=1:\quad \frac{\partial\widetilde{V}_{z0}}{\partial z}=0, \tag{4.9}$$

where (4.9) is obtained from (2.11) and use of (4.2), (4.4), and (4.5). The simplicity of the equation can be attributed to the large-aspect-ratio condition $\delta\gg 1$.

The general solution for $\widetilde{V}_{z0}$ is

$$\widetilde{V}_{z0}(z,t)=A\sin\omega t+\sum_{n=0,n\neq n^*}^{\infty}\frac{2A\omega}{b_n^2-\omega^2}\left(\frac{\omega}{b_n}\sin\omega t-\sin b_n t\right)\sin b_n z$$
$$-\left(\left(\frac{1}{b_{n^*}}\right)\sin b_{n^*}t+t\cos b_{n^*}t\right)\sin b_{n^*}z, \tag{4.10}$$

where $b_n=(n+\frac{1}{2})\pi$. The last term describes a resonant effect present only when $\omega=b_{n^*}$ and cannot be found from a quasi-steady analysis. The solution provides

https://doi.org/10.1017/S0022112000008454 Published online by Cambridge University Press

ω	ω'(Hz)	Properties	Primary response
1	159	stable	axial + quasi-steady modes
1.4	223	beats	quasi-steady modes
$\pi/2$	250	axial amplification	linear growth

TABLE 1. Acoustic response properties for several driving frequencies.

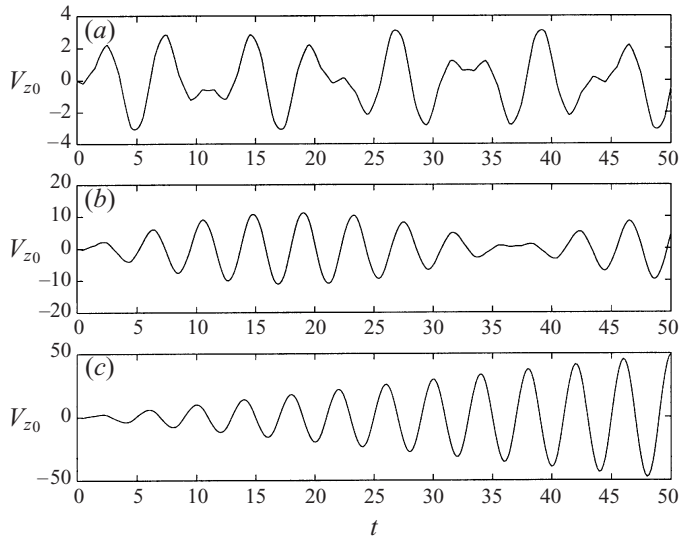


FIGURE 2. Acoustic velocity, $\widehat{V}_{z0}$ in the core of the cylinder at $z = 0.5$ for three difference oscillation frequencies: $\omega = 1$ (a), $\omega = 1.4$ (b), and $\omega = \pi/2$ (c).

insight into the properties of the acoustical field compatible with the cylindrical geometry and prescribed boundary conditions.

(i) The first term itself and the second part of the non-resonant Fourier series represent quasi-steady motion at the driving frequency. The other Fourier series terms can each be decomposed into two counter-propagating planar travelling waves.

(ii) If ω is very close to one of the natural frequencies, then beats will appear due to the interaction between the quasi-steady motion and one pair of travelling waves.

(iii) Resonance occurs when $\omega = b_n$, and the amplitude of one mode grows linearly with time.

Table 1 contains results for a system where $t'_A = 10^{-3}$ s, so that dimensional frequencies can be considered. When $\omega' \approx 159$ Hz, the response shown in figure 2(a) for $\widetilde{V}_{z0}$ at $z = 0.5$ is bounded and the contributions are primarily from the first few forced modes and the first few axial travelling modes. A beat is observed in figure 2(b) when $\omega' \approx 223$ Hz, and A is chosen to be 1. The period of the beat, about 45 time units, arises from the interaction between the driven frequency $\omega = 1.4$ and the first eigenfunction $b_0 = \pi/2$. Linear monotonic amplitude growth seen in figure 2(c) is primarily from the resonant axial mode in (4.10) when $\omega' = 250$ Hz ($\omega = b_0 = \pi/2$).

The pressure solution $P_0(z, t)$ can be obtained from a first integral of the unsteady part of (4.2) and the isentropic relationship $P_0 = \gamma\rho_0$.

https://doi.org/10.1017/S0022112000008454 Published online by Cambridge University Press

4.2. *Transition layer solution*

The leading-order core acoustic solution in (4.10) does not satisfy the no-slip boundary condition. Under certain conditions, to be defined quantitatively, the transition to zero axial velocity at the wall occurs in a relatively thin transition layer which has a multiple-scale structure that differs fundamentally from a traditional viscous acoustic boundary layer (Flandro 1974). In particular the overall radial thickness of the layer is defined by weak viscous considerations. But within it there is a smaller length scale associated with the distance travelled by an injected fluid particle on the time scale $t'_A = L'/C'_0$.

The fast injection condition $V'_{r0} \gg V'_{z0}/Re^{1/2}$ implies that the transition layer is inviscid and rotational in the first approximation. Viscous stresses appear in a higher-order description, but are essential to finding the complete solution, as might be expected in a multiple-scale analysis.

The multiple-scale structure is defined in terms of stretched variables that measure distance from the tube wall:

$$\xi = \frac{1-r}{M}, \qquad \eta = \frac{1-r}{\beta}, \tag{4.11}$$

where $\beta = M^2/(\delta^2/Re)$ if the core/transition layer concept is valid. In order for the total layer thickness to be large compared to the smaller-scale feature but small compared to the tube radius, $M \ll \beta \ll 1$. The partial derivatives with respect to r must be replaced by

$$\left.\begin{aligned} \left(\frac{\partial}{\partial r}\right) &= -\frac{1}{M}\left(\frac{\partial}{\partial \xi}\right) - \frac{1}{\beta}\left(\frac{\partial}{\partial \eta}\right), \\ \left(\frac{\partial^2}{\partial r^2}\right) &= \frac{1}{M^2}\left(\frac{\partial^2}{\partial \xi^2}\right) + \frac{2}{M\beta}\left(\frac{\partial^2}{\partial \eta \partial \xi}\right) + \frac{1}{\beta^2}\left(\frac{\partial^2}{\partial \eta^2}\right). \end{aligned}\right\} \tag{4.12}$$

The variables, represented by the asymptotic expansions

$$\left.\begin{aligned} (P, \rho, T) &\sim 1 + \sum_{n=0} M^{n+1}(P_n, \rho_n, T_n), \\ V_z &\sim V_{z0} + \frac{M}{\beta} V_{z1} + o\left(\frac{M}{\beta}\right), \\ V_r &\sim -V_{rw}(z) + o(1), \end{aligned}\right\} \tag{4.13}$$

valid in the limit $M \to 0$, are used with (4.12) in (2.1)–(2.5) to find the first two approximate equation systems for the transition layer.

The lowest-order version is

$$\frac{\partial V_{z0}}{\partial t} + V_{rw}\frac{\partial V_{z0}}{\partial \xi} = -\frac{1}{\gamma}\frac{\partial P_0}{\partial z}, \tag{4.14}$$

$$P_0 = P_0(z, t), \tag{4.15}$$

where $V_{rw}(z)$ is known from (2.9) and $P_0(z, t)$ is the acoustic pressure field obtained from (4.2) and (4.10). Equation (4.14) describes an inviscid rotational flow which can satisfy the no-slip boundary condition on the wall. In particular, an evaluation of (4.14) on the wall $\xi = \eta = 0$ shows that the transient vorticity distribution created there,

$$\left(\frac{\partial V_{z0}}{\partial \xi}\right)_w = -\frac{1}{\gamma V_{rw}(z)}\frac{\partial P_0(z, t)}{\partial z}, \tag{4.16}$$

https://doi.org/10.1017/S0022112000008454 Published online by Cambridge University Press

depends on both the local pressure gradient time variation and the local injection magnitude. This transition layer vorticity is $O(M^{-1})$ larger than that associated with the steady solution in (3.5)–(3.7), given the stretching transformation in the first of (4.11).

The convective transport equation for the relatively intense transient vorticity, $\partial V_{z0}/\partial\xi$, can be obtained from a ξ-derivative of (4.14). In this case, the right-hand side vanishes and one finds that vorticity is convected invariantly by the radial wall injection velocity V_{rw} along well-defined characteristic lines, $\varphi = t - (\xi/V_{rw})$.

The second-order momentum equation is obtained from terms of $O(M/\beta)$,

$$\frac{\partial V_{z1}}{\partial t} + V_{rw}\frac{\partial V_{z1}}{\partial \xi} = -V_{rw}\frac{\partial V_{z0}}{\partial \eta} + \frac{\partial^2 V_{z0}}{\partial \xi^2}, \tag{4.17}$$

where a viscous stress term associated with V_{z0} is present, and the pressure gradient is absent since $\beta \ll 1$.

The acoustic solution in the core must match with the transition layer solutions at the outer edge ($\xi \to \infty, \eta \to \infty$), based on familiar principles in the theory of matched asymptotic expansion (see Cole & Kevorkian 1996). The no-slip condition on the sidewall provides an inner boundary condition for (4.14) and (4.17). The acoustic core solution in (4.10) shows that all the terms can be classified into the following two forms: $\overline{V}_{z0}(z)\mathrm{e}^{\mathrm{i}\Omega t}$ with $\Omega = \omega$ or b_n, $\overline{V}_{z0}(z) = \sin b_n z$, and $-t\cos(b_{n^*}t)\sin(b_{n^*}z)$. It follows that

$$\xi = \eta = 0: \quad V_{z0} = 0, \tag{4.18}$$

$$\xi, \eta \to \infty: \quad V_{z0} \sim \widetilde{V}_{z0}(z,t), \tag{4.19}$$

with the latter from (4.10).

Equations (4.14)–(4.19) are used first to find quasi-steady solutions to each relevant frequency in the core solution. For any of the non-resonant modes $\Omega = \omega$ or b_n but $\omega \neq b_n$ for any integer n, the transition layer solutions can be written as

$$V_{z0} = F(\xi,\eta,z)\mathrm{e}^{\mathrm{i}\Omega t}, \qquad V_{z1} = G(\xi,\eta,z)\mathrm{e}^{\mathrm{i}\Omega t}. \tag{4.20}$$

These solution forms can be substituted into (4.14) and (4.17) to determine F and G. The former found from (4.14), (4.18) and (4.19), is

$$F(\xi,\eta,z) = C(\eta,z)\exp\left(-\frac{\mathrm{i}\Omega}{V_{rw}}\xi\right) + \overline{V}_{z0} \tag{4.21}$$

where the undetermined coefficient function $C(\eta,z)$ must satisfy the conditions

$$\eta = 0: \quad C = -\overline{V}_{z0}(z), \tag{4.22}$$

$$\eta \longrightarrow \infty: \quad C = 0. \tag{4.23}$$

Equation (4.14) can then be rewritten in terms of G and C as

$$\frac{\partial G}{\partial \xi} + \frac{\mathrm{i}\Omega}{V_{rw}}G = -\exp\left(-\frac{\mathrm{i}\Omega}{V_{rw}}\xi\right)\left[\frac{\partial C}{\partial \eta} + \frac{\Omega^2}{V_{rw}^3}C\right] \tag{4.24}$$

where the second term in the square brackets arises from viscous effects.

In order to avoid secular growth of G with respect to the variable ξ, the quantities in the square bracket must be set to zero. Therefore,

$$\frac{\partial C}{\partial \eta} + \frac{\Omega^2}{V_{rw}^3}C = 0, \tag{4.25}$$

https://doi.org/10.1017/S0022112000008454 Published online by Cambridge University Press

which together with (4.22)–(4.23) is solved to find

$$C(\eta, z) = -\overline{V}_{z0} \exp\left(-\frac{\Omega^2}{V_{rw}^3}\eta\right). \tag{4.26}$$

It follows that the axial velocity variation in the transition layer for each frequency Ω has the form

$$V_{z0}(\xi, \eta, z, t) = -\sin(b_n z)\left\{\exp\left[-\frac{\Omega^2}{V_{rw}^3(z)}\eta - \frac{\mathrm{i}\Omega}{V_{rw}(z)}\xi\right] - 1\right\}\mathrm{e}^{\mathrm{i}\Omega t} \tag{4.27}$$

where $-V_{rw}(z)$ is the steady sidewall injection velocity. The product of the exponential terms in (4.27) yields that part of the axial velocity component containing the intense transient vorticity of the transition layer:

$$\exp\left(-\frac{\Omega^2}{V_{rw}^3(z)}\eta\right)\mathrm{e}^{\mathrm{i}\Omega\varphi} \tag{4.28}$$

where $\varphi = t - \xi/V_{rw}$ is the characteristic line for vorticity transport. The radial travelling speed for a constant-φ line can be described by

$$\left.\frac{\partial r}{\partial t}\right|_{\varphi} = -M\left.\frac{\partial \xi}{\partial t}\right|_{\varphi} = -MV_{rw}(z). \tag{4.29}$$

This shows explicitly that the vorticity is convected in the transition layer by the steady wall injection speed.

The first factor in (4.28) describes amplitude damping arising from viscous effects because the η-variable defined in (4.11) is scaled with respect to Re, in part. The second part describes harmonic spatial oscillations associated with the acoustic solution in the core.

When resonant driving is present $\Omega = \omega = b_{n^*}$, and the resonant mode representation of V_{z0} is found in a similar way to be

$$\begin{aligned} V_{z0}(\xi, \eta, z, t) = {} & -t\sin(b_{n^*}z)\sin(b_{n^*}t) + \Bigg\{ t\left[\sin(k\xi)\sin(b_{n^*}t) + b_{n^*}\cos(k\xi)\cos(b_{n^*}t)\right] \\ & - \left[\frac{\eta}{(1+b_{n^*})}\cos(k\xi) + \frac{b_{n^*}\xi}{2k^2(1+b_{n^*})}\sin(k\xi)\right]\sin(b_{n^*}t) \\ & - \frac{1}{\omega}\left[\frac{V_{rw}^2(z)}{2(1+b_{n^*})}\xi\cos(k\xi) - \left(1 - \frac{b_{n^*}^2}{1+b_{n^*}}\right)\sin(k\xi)\right]\cos(b_{n^*}t)\Bigg\} \\ & \times \frac{1}{b_{n^*}}\sin(b_{n^*}z)\exp\left(-\frac{b_{n^*}^2}{V_{rw}^3(z)}\eta\right) \end{aligned} \tag{4.30}$$

where $k = b_{n^*}/V_{rw}(z)$.

When $\xi = \eta = 0$, the solutions satisfy the no-slip boundary condition on the wall. On the other hand, when ξ and $\eta \to \infty$, the core solution is recovered in an oscillatory manner since the amplitude of the exponential term goes to zero harmonically. The effective thickness of the transition layer depends strongly on Ω and V_{rw}. A large value of Ω promotes relatively rapid exponential decay, implying that a high-frequency disturbance is associated with a thinner transition layer. Alternatively, low-frequency forcing fosters thick transition layers. Thus, higher-order modes tend to be associated with effectively thinner transition layers. The same type of argument demonstrates that increasing the value of $V_{rw}(z)$ enhances the overall transition layer thickness.

Figure 3 gives a graphical representation of the transition layer. This shows that

https://doi.org/10.1017/S0022112000008454 Published online by Cambridge University Press

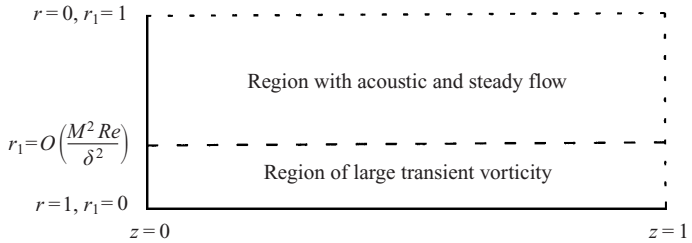


FIGURE 3. The regions of interest for the problem in § 4. The region between the sidewall $r = 1$ and the dashed line at $r_1 = O(M^2Re/\delta^2) \ll 1$ is characterized by fluid with large $(O(1/M))$ transient vorticity. The region between $r_1 = O(M^2Re/\delta^2) \ll 1$ and the centreline at $r = 0$ is characterized by purely acoustic flow. The vorticity generated at the sidewall decays as the edge of the transition layer is approached. Both regions are also characterized by the steady flow conditions as described in (3.5)–(3.7).

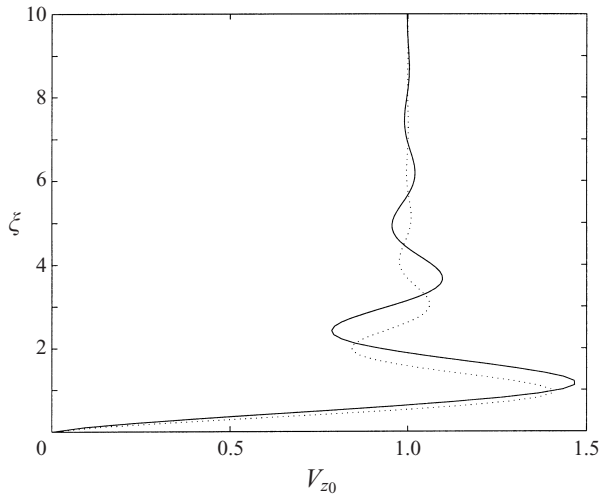


FIGURE 4. The axial velocity in the transition layer as a function of ξ for $M = 0.01$, $\beta = 0.1$, when $\Omega = 2.5$ for the solid curve and $\Omega = 3$ for the dotted curve. The boundary layer is thicker for the smaller frequency value.

the region of high transient vorticity is adjacent to the sidewall and confined to a thin region of thickness $\beta = M^2Re/\delta^2$. The magnitude of the vorticity decays from its source at the sidewall as it convects toward the centreline. The area between the edge of the vortical region is characterized by the acoustic flow described by (4.10) and the steady flow of (3.5)–(3.7).

A complete solution for the axial velocity in the transition layer consists of an infinite sum of terms obtained from (4.27) and (4.30), one for each frequency ω and b_n in (4.10). The spatial structure of such a solution will be quite complex, given the oscillatory dependence on the value of Ω. It is perhaps more illustrative to look at the results for a single frequency.

The reduced axial velocity inside the vortical layer, $V_{z0}/[-\overline{V}_{z0}e^{i\Omega t}]$ is plotted against ξ in figure 4 with $M = 0.01$, $\beta = 0.1$ and $V_{rw} = 1$ for $\Omega = 2.5$ and $\Omega = 3.0$. The core solution is recovered at about $\xi = 10$ for $\Omega = 2.5$ which corresponds to $r = 0.9$. In contrast, the transition layer thickness is a little smaller for the higher frequency

https://doi.org/10.1017/S0022112000008454 Published online by Cambridge University Press

$\Omega = 3.0$. Of course the overall transition layer thickness is determined by the lowest mode in the system.

The viscous factors in (4.27) and (4.30) decay exponentially at the edge of the transition layer when $\eta \to \infty$. In dimensional terms, the layer thickness can be characterized by the decay length $l_D' = (\beta V_{rw}^3/\Omega^2)R'$ obtained from the dimensional form of the argument of the exponential in (4.28) or the analogous term in (4.30). This result, noted initially by Zhao (1994), has been reconfirmed by Majdalani (1998) in a study of linear, quasi-steady stability employing the unusual asymptotic methods described by Majdalani & Van Moorhem (1997). In order to assure the existence of a thin transition layer, $l_D'/R' = \beta V_{rw}^3/\Omega^2 \ll 1$. Given the definition of β below (4.11), and that the characteristic injection Mach number can be defined by $M_b = M/\delta$, it follows that $\beta = M_b^3 \delta R_A$, where the acoustic Reynolds number $R_A \equiv Re/M$. This shows explicitly that an increase in the characteristic wall injection Mach number will eventually cause the transition layer to be as large as the cylinder radius, $l_D' = O(R')$ or $\beta = O(1)$, so that the core/transition layer concept fails. Then a new multiple-scale perturbation technique is needed to find solutions where rotational effects co-exist with an acoustic field throughout the cylinder.

5. Co-existing acoustic/rotational flow

The failure of the core/transition layer asymptotic model, described in § 4, when $\beta = O(1)$ implies that one must develop a mathematical model for co-existing acoustic and rotational disturbances of equal magnitude. Flandro (1995*a*) describes a theoretical formulation for such a situation when the amplitude of the transients is smaller than that of the steady Culick (1966) profiles in (3.5)–(3.7). Perturbation methods valid for $M_b \to 0$ are used to derive an *inviscid* linear equation for the rotational part of the transient axial velocity component. Although the importance of a shorter radial length scale is recognized, a formal multiple-length-scale analysis is not employed. Further, an intuitive approach is used to determine which terms in the full equations are retained in the lowest order asymptotic analysis. The solution driven by a quasi-steady acoustic field, satisfies the no-slip condition on the sidewall and symmetry conditions at the cylinder axis. It is characterized by harmonically varying shear waves on the short length scale that are convected into the cylinder by the Culick (1966) steady velocity components. The viscous damping of earlier work of Flandro (1974), like that observed in (4.27) or (4.28), is replaced by a non-viscous attenuation function associated with the axial dependence of the acoustic velocity field.

Here, an alternative formulation is developed based on a systematic, fully defined multiple-scale analysis that includes the effects of weak viscosity. The asymptotic expansions for the velocity components and thermodynamic variables in the limit $M \to 0$ are

$$\left.\begin{aligned} V_r &\sim V_{r0s}(z,r) + \sum_{n=0} M^n \widetilde{V}_{rn}(z,r,t), \\ V_z &\sim V_{z0s}(z,r) + \sum_{n=0} M^n \widetilde{V}_{zn}(z,r,t), \\ (P,\rho,T) &\sim 1 + M \sum_{n=0} M^n (\widetilde{P}_n, \widetilde{\rho}_n, \widetilde{T}_n), \end{aligned}\right\} \tag{5.1}$$

where the axial speed transient disturbances are as large as the Culick (1966) profiles. The terms V_{r0s} and V_{z0s} in the first terms of (5.1) are the steady solutions in (3.5) and (3.6). The tilde on the second terms denotes unsteady variables.

https://doi.org/10.1017/S0022112000008454 Published online by Cambridge University Press

It is recognized that two disparate length scales are important: the tube radius and a much shorter length associated with the radial distance travelled by a fluid particle on the acoustic time scale. A multiple-scale analysis will be carried out in terms of the variables r_1 and r_2 defined by

$$r_1 = 1 - r, \qquad r_2 = \int_0^{r_1} \frac{1}{-MV_{r0s}(\sigma)} \mathrm{d}\sigma. \tag{5.2}$$

The second transformation, used first in Zhao & Kassoy (1994), includes an integral of the steady radial velocity field for the case of constant steady wall injection $V_{rw} = 1$. The integral transformation simplifies the equations considerably. It is noted that when the centreline is approached, $r_1 \to 1$, the integral diverges and $r_2 \to \infty$.

Each of the dependent variables is written in terms of r_1 and r_2 instead of r alone. The partial derivatives with respect to r in equations (2.1)–(2.5) must be replaced by

$$\left.\begin{aligned} \frac{\partial}{\partial r} &\to -\frac{\partial}{\partial r_1} + \frac{1}{MV_{r0s}}\frac{\partial}{\partial r_2}, \\ \frac{\partial^2}{\partial r^2} &\to \frac{\partial^2}{\partial r_1^2} - \frac{2}{MV_{r0s}}\frac{\partial^2}{\partial r_1 \partial r_2} + \left(\frac{1}{MV_{r0s}}\right)^2 \frac{\partial^2}{\partial r_2^2} + \frac{1}{MV_{r0s}^2}\frac{\partial V_{r0s}}{\partial r_1}\frac{\partial}{\partial r_2}. \end{aligned}\right\} \tag{5.3}$$

5.1. *Lowest-order mathematical model*

The relations in (5.1) can be substituted into (2.1)–(2.5) to find the leading-order equations in the limit $M \to 0$. First, the spatially homogeneous boundary forcing in (2.12) and the condition $\delta \gg 1$ imply that $\widetilde{V}_{r0} = 0$. Then,

$$\frac{\partial \widetilde{\rho}_0}{\partial t} + \frac{\partial \widetilde{\rho}_0}{\partial r_2} = -\frac{\partial \widetilde{V}_{z0}}{\partial z} - \frac{1}{V_{r0s}}\frac{\partial \widetilde{V}_{r1}}{\partial r_2}, \tag{5.4}$$

$$\frac{\partial \widetilde{P}_0}{\partial r_1} = \frac{\partial \widetilde{P}_0}{\partial r_2} = 0, \tag{5.5}$$

$$\frac{\partial \widetilde{V}_{z0}}{\partial t} + \frac{\partial \widetilde{V}_{z0}}{\partial r_2} = -\frac{1}{\gamma}\frac{\partial \widetilde{P}_0}{\partial z}, \tag{5.6}$$

$$\frac{\partial \widetilde{T}_0}{\partial t} + \frac{\partial \widetilde{T}_0}{\partial r_2} = \frac{\gamma - 1}{\gamma}\frac{\partial \widetilde{P}_0}{\partial t}, \tag{5.7}$$

$$\widetilde{P}_0 = \widetilde{\rho}_0 + \widetilde{T}_0. \tag{5.8}$$

Following a procedure related to that described by Lagerstrom (1964), and similar to that employed by Flandro (1995*a*), the variables, except for $\widetilde{P}_0$, are divided into co-existing irrotational planar and rotational non-planar parts of equal magnitude,

$$\left.\begin{aligned} \widetilde{V}_{z0} &= \overline{V}_{z0}(z,t) + \widehat{V}_{z0}(z,t,r_1,r_2), \\ \widetilde{\rho}_0 &= \overline{\rho}_0(z,t) + \widehat{\rho}_0(z,t,r_1,r_2), \\ \widetilde{T}_0 &= \overline{T}_0(z,t) + \widehat{T}_0(z,t,r_1,r_2), \end{aligned}\right\} \tag{5.9}$$

where the overbar denotes irrotational (planar) variables and the hat denotes rotational variables.

The expansions in (5.9) can be used in (5.4)–(5.8) to show that the planar functions

https://doi.org/10.1017/S0022112000008454 Published online by Cambridge University Press

are described by an irrotational acoustic system

$$\frac{\partial \overline{\rho}_0}{\partial t} = -\frac{\partial \overline{V}_{z0}}{\partial z}, \tag{5.10}$$

$$\widetilde{P}_0 = \widetilde{P}_0(z,t), \tag{5.11}$$

$$\frac{\partial \overline{V}_{z0}}{\partial t} = -\frac{1}{\gamma}\frac{\partial \widetilde{P}_0}{\partial z}, \tag{5.12}$$

$$\frac{\partial \overline{T}_0}{\partial t} = \frac{\gamma-1}{\gamma}\frac{\partial \widetilde{P}_0}{\partial t}, \tag{5.13}$$

$$\widetilde{P}_0 = \overline{\rho}_0 + \overline{T}_0, \tag{5.14}$$

nearly identical to (4.2)–(4.5).

The initial/boundary conditions are

$$t = 0: \quad \overline{V}_{z0} = 0, \quad \frac{\partial \overline{V}_{z0}}{\partial t} = 0, \tag{5.15}$$

$$z = 0: \quad \overline{V}_{z0} = A\sin\omega t, \tag{5.16}$$

$$z = 1: \quad \frac{\partial \overline{V}_{z0}}{\partial z} = 0, \tag{5.17}$$

in analogy to (4.7)–(4.9).

The non-resonant acoustic solution for $\overline{V}_{z0}$ is the same as the core solution in (4.10),

$$\overline{V}_{z0}(t,z) = A\sin\omega t + \sum_{n=0,n\neq n^*}^{\infty} \frac{2A\omega}{b_n^2-\omega^2}\left(\frac{\omega}{b_n}\sin\omega t - \sin b_n t\right)\sin b_n z, \tag{5.18}$$

where $b_n = (n+\frac{1}{2})\pi$ for $\omega \neq b_n$. The pressure $\widetilde{P}_0$ is found using (5.12) and the boundary condition in (2.11),

$$\widetilde{P}_0(t,z) = A\gamma\omega(z-1)\cos\omega t - \sum_{n=0}^{\infty}\frac{2A\omega}{b_n^2}(\cos\omega t - \cos b_n t)\cos b_n z, \tag{5.19}$$

and the thermodynamic variables $\overline{T}_0$ and $\widetilde{P}_0$,

$$\overline{T}_0 = \frac{\gamma-1}{\gamma}\widetilde{P}_0, \tag{5.20}$$

$$\overline{\rho}_0 = \frac{1}{\gamma}\widetilde{P}_0. \tag{5.21}$$

The first term in the sums of (5.18) and (5.19) arises from forcing at frequency ω, and the second term describes the eigenfunction response. Only the non-resonant case will be considered in the present work.

The equations for the rotational components are

$$\frac{\partial \widehat{\rho}_0}{\partial t} + \frac{\partial \widehat{\rho}_0}{\partial r_2} = -\frac{\partial \widehat{V}_{z0}}{\partial z} - \frac{1}{V_{r0s}}\frac{\partial \widetilde{V}_{r1}}{\partial r_2} \tag{5.22}$$

$$\frac{\partial \widehat{V}_{z0}}{\partial t} + \frac{\partial \widehat{V}_{z0}}{\partial r_2} = 0, \tag{5.23}$$

https://doi.org/10.1017/S0022112000008454 Published online by Cambridge University Press

$$\frac{\partial \widehat{T}_0}{\partial t} + \frac{\partial \widehat{T}_0}{\partial r_2} = 0, \tag{5.24}$$

$$\widehat{\rho}_0 + \widehat{T}_0 = 0. \tag{5.25}$$

Equations (5.24) and (5.25) can be combined to show that the leading-order rotational density is described by

$$\frac{\partial \widehat{\rho}_0}{\partial t} + \frac{\partial \widehat{\rho}_0}{\partial r_2} = 0. \tag{5.26}$$

Therefore, (5.22) can be rewritten as

$$\frac{\partial \widehat{V}_{z0}}{\partial z} + \frac{1}{V_{r0s}} \frac{\partial \widetilde{V}_{r1}}{\partial r_2} = 0, \tag{5.27}$$

which can be used to find the r_2-dependence of $\widetilde{V}_{r1}$ once $\widehat{V}_{z0}$ is known.

The relevant initial and boundary conditions are

$$t = 0: \quad \widehat{V}_{z0} = 0, \quad \frac{\partial \widehat{V}_{z0}}{\partial t} = 0, \tag{5.28}$$

$$z = 0: \quad \widehat{V}_{z0} = 0, \tag{5.29}$$

$$r_1 = 1, \ r_2 \to \infty: \quad \frac{\partial \widehat{V}_{z0}}{\partial r_2} = 0, \quad \frac{\partial \widehat{T}_0}{\partial r_2} = 0, \tag{5.30}$$

$$r_1 = r_2 = 0: \quad \widehat{V}_{z0} = -\overline{V}_{z0}(t, z), \quad \widehat{T}_0 = -\overline{T}_0(t, z). \tag{5.31}$$

The first of (5.30) can be combined with (5.23) and the initial condition (5.28) to prove that $\widehat{V}_{z0} = 0$ on the axis $r_1 = 0$ for all t. Equation (5.31) corresponds to the no-slip condition and isothermal flow injection. Equations (5.23), (5.24) and (5.26) show that $\widehat{V}_{z0}$, $\widehat{T}_0$ and $\widehat{\rho}_0$ are invariant on a characteristic line defined by

$$\eta = t - r_2, \tag{5.32}$$

but vary across the η lines. On the sidewall ($r_2 = 0$), the $\eta = 0$ line appears at $t = 0^+$ and subsequently, at $t = c > 0$, $\eta = c$ appears. At a particular time τ, constant-η lines, which range in value from 0 to τ, are transported toward the axis by convection at the local radial steady velocity, as found from a time derivative of (5.32) after using (5.2).

The inviscid equation in (5.23) can be combined with the first of (5.31) and (5.12) to show that vorticity is produced on the sidewall by the transient axial gradient of the acoustic pressure field,

$$\frac{\partial \widehat{V}_{z0}(t, z, 0, 0)}{\partial r_2} = -\frac{\partial \widehat{V}_{z0}}{\partial t} = \frac{\partial \overline{V}_{z0}}{\partial t} = -\frac{1}{\gamma} \frac{\partial \widetilde{P}_0}{\partial z}, \tag{5.33}$$

where $\overline{V}_{z0}$ and $\widetilde{P}_0$ are given in (5.18) and (5.19). Equation (5.33) is analogous to (4.16) in the core/transition layer description. It is noted that the largest unsteady non-dimensional vorticity term is given by

$$\widetilde{\Omega}_\theta = \left(\frac{1}{M V_{r0s}} \right) \frac{\partial \widehat{V}_{z0}}{\partial r_2}. \tag{5.34}$$

The parameter, $1/M$, arises from large gradients occurring in the spatially oscillatory velocity profile on the short length scale r_2. Equation (5.23) also shows that the

https://doi.org/10.1017/S0022112000008454 Published online by Cambridge University Press

vorticity generated at the wall is convected into the cylinder by the steady radial velocity field $V_{r0s}(r)$.

It should be noted that the inviscid equation for $\widehat{V}_{z0}$ in (5.23) differs from the analogous equation of Flandro (1995*a*) which includes an axial convection term proportional to $\partial \widehat{V}_{z0}/\partial z$, retained on the basis of an intuitive rather than a formal asymptotic argument.

In general, solutions to the inviscid first-order hyperbolic equations in (5.23) and (5.24) can be written formally as

$$\widehat{V}_{z0} = \widehat{V}_{z0}(\eta, r_1, z), \qquad \widehat{T}_0 = \widehat{T}_0(\eta, r_1, z) = -\widehat{\rho}_0, \qquad \eta = t - r_2. \tag{5.35}$$

If the no-slip and isothermal boundary conditions (see (2.9) and (5.31)) are satisfied, then one finds results on $r_1 = 0$:

$$\widehat{V}_{z0}(\eta, 0, z) = -\overline{V}_{z0}(\eta, z), \qquad \widehat{T}_0(\eta, 0, z) = -\frac{(\gamma - 1)}{\gamma}\widetilde{P}_0(\eta, z), \tag{5.36}$$

where the quantities on the right-hand side of the equality signs are given in (5.18) and (5.19). The results in (5.36) are essentially boundary conditions for higher-order equations, which are used to find explicit functional dependence of the variables. Once $\widehat{V}_{z0}$ is found, then the mass conservation equation (5.27) can be integrated with respect to r_2 to find the r_2-dependence of the radial velocity $\widehat{V}_{r1}$.

The r_1-dependence of the rotational temperature field is described in (5.24), and is analogous to the axial rotational velocity in (5.23). The solution to (5.24) can be found along the characteristics in (5.32), the same as those found for the rotational axial velocity. Similarly to that of the vorticity along the sidewall in (5.33), the heat flux can also be found along the sidewall. Details on this procedure can be found in Staab *et al.* (1999).

5.2. *Higher-order considerations*

The expansions in (5.1) can be combined with (2.1)–(2.5) to find the $O(M)$ equation set in the limit $M \to 0$. The procedure used to find the leading-order solution is employed so that the variables, except for $\widetilde{P}_1$, are divided into irrotational planar and rotational non-planar parts,

$$\left.\begin{aligned} \widetilde{V}_{z1} &= \overline{V}_{z1}(z,t) + \widehat{V}_{z1}(z,t,r_1,r_2), \\ \widetilde{\rho}_1 &= \overline{\rho}_1(z,t) + \widehat{\rho}_1(z,t,r_1,r_2), \\ \widetilde{T}_1 &= \overline{T}_1(z,t) + \widehat{T}_1(z,t,r_1,r_2). \end{aligned}\right\} \tag{5.37}$$

The planar, acoustic equations,

$$\frac{\partial \overline{\rho}_1}{\partial t} = -\frac{\partial}{\partial z}\left(\overline{V}_{z1} + \overline{\rho}_0 \overline{V}_{z0}\right), \tag{5.38}$$

$$\frac{\partial \overline{V}_{z1}}{\partial t} = \frac{\partial}{\partial z}\left(-\frac{1}{\gamma}\left(\widetilde{P}_1 - P_{0s}\right) + \frac{\overline{\rho}_0^2}{2} - \frac{\overline{V}_{z0}^2}{2}\right), \tag{5.39}$$

$$\frac{\partial \overline{T}_1}{\partial t} = \frac{\partial}{\partial t}\left((\gamma - 1)\overline{\rho}_1 + \frac{(\gamma - 2)(\gamma - 1)}{2}\overline{\rho}_0^2\right), \tag{5.40}$$

$$\widetilde{P}_1 = \overline{\rho}_1 + \overline{T}_1 + \overline{\rho}_0 \overline{T}_0, \tag{5.41}$$

https://doi.org/10.1017/S0022112000008454 Published online by Cambridge University Press

containing quadratic driving terms associated with lower-order acoustics are not considered further here, although they may be important for studying acoustic streaming effects.

The largest possible viscous effect occurs when $\beta = ReM^2/\delta^2 = O(1)$ (see (4.11)), in which case the higher-order axial momentum equation for $\widehat{V}_{z1}$ has the non-homogeneous form

$$\frac{\partial \widehat{V}_{z1}}{\partial t} + \frac{\partial \widehat{V}_{z1}}{\partial r_2} = \frac{1}{V_{r0s}^2}\frac{\partial^2 \widehat{V}_{z0}}{\partial r_2^2} + \frac{1}{\gamma}\widehat{\rho}_0\frac{\partial \widetilde{P}_0}{\partial z} + \frac{\widetilde{V}_{r1}}{V_{r0s}}\frac{\partial \widehat{V}_{z0}}{\partial r_2} + V_{r0s}\frac{\partial \widehat{V}_{z0}}{\partial r_1} - \widehat{V}_{z0}\left(\frac{\partial V_{z0s}}{\partial z} + \frac{\partial \overline{V}_{z0}}{\partial z} + \frac{\partial \widehat{V}_{z0}}{\partial z}\right) - \left(\overline{V}_{z0s} + V_{z0s}\right)\frac{\partial \widehat{V}_{z0}}{\partial z}. \quad (5.42)$$

Equation (5.42), the higher-order analogue to (5.23), provides additional information about the behaviour of the leading-order axial speed solution.

If the transformation of the coordinate system from (t, r_1, r_2, z) to (η, r_1, r_2, z) is made, then the derivatives with respect to t and r_2 must be replaced by

$$\left(\frac{\partial}{\partial t}\right) = \left(\frac{\partial}{\partial \eta}\right)_{r_2}, \qquad \left(\frac{\partial}{\partial r_2}\right) = \left(\frac{\partial}{\partial r_2}\right)_{\eta} - \left(\frac{\partial}{\partial \eta}\right)_{r_2}. \quad (5.43)$$

It follows that (5.42) can be written as

$$\left.\frac{\partial \widehat{V}_{z1}}{\partial r_2}\right|_{\eta} = \frac{1}{V_{r0s}^2}\frac{\partial^2 \widehat{V}_{z0}}{\partial \eta^2} + V_{r0s}\frac{\partial \widehat{V}_{z0}}{\partial r_1} + \frac{1}{\gamma}\widehat{\rho}_0\frac{\partial \widetilde{P}_0}{\partial z} - \frac{1}{V_{r0s}}\left(\frac{\partial (V_{r1}\widehat{V}_{z0})}{\partial r_2} - \frac{\partial (V_{r1}\widehat{V}_{z0})}{\partial \eta}\right) - \widehat{V}_{z0}\left(\frac{\partial V_{z0s}}{\partial z} + \frac{\partial \overline{V}_{z0}}{\partial z} + \frac{\partial \widehat{V}_{z0}}{\partial z}\right) - \left(\overline{V}_{z0s} + V_{z0s}\right)\frac{\partial \widehat{V}_{z0}}{\partial z}. \quad (5.44)$$

An integration of (5.44) with respect to r_2, holding η, r_1 and z fixed will generate secular growth in r_2 unless certain terms are suppressed. Details of a similar analysis are given in Staab (1998). In considering the impact of each term, it is important to remember that the harmonic t-dependence of the planar acoustic solutions in (5.18)–(5.21) must be rewritten in terms of η and r_2 by using (5.32). When written in the coordinate system (z, t, r_1, r_2) the suppressed terms take the form

$$\frac{1}{V_{r0s}^2}\frac{\partial^2 \widehat{V}_{z0}}{\partial r_2^2} + V_{r0s}\frac{\partial \widehat{V}_{z0}}{\partial r_1} - \frac{\partial}{\partial z}\left(\tfrac{1}{2}\widehat{V}_{z0}^2 + \widehat{V}_{z0}V_{z0s}\right) = 0, \quad (5.45)$$

which is a nonlinear diffusion equation for the rotational axial velocity $\widehat{V}_{z0}$ with a time-like variable r_1. Equation (5.45) is a balance of viscous diffusion on the r_2-scale, transport of axial momentum by the steady radial speed and nonlinear axial convection. The solution for $\widehat{V}_{z0}$ must satisfy an 'initial' condition at $r_1 = 0$ from (5.31),

$$\left.\widehat{V}_{z0}\right|_{r_1=0} = \begin{cases} -\overline{V}_{z0}(\eta, z) = -A\sin\omega\eta - \displaystyle\sum_{n=0}^{\infty}\frac{2A\omega}{b_n^2 - \omega^2}\left(\frac{\omega}{b_n}\sin\omega\eta - \sin b_n\eta\right)\sin b_n z, & \eta > 0 \\ 0, & \eta < 0, \end{cases} \quad (5.46)$$

https://doi.org/10.1017/S0022112000008454 Published online by Cambridge University Press

and a boundary condition at the centreline from (5.30)

$$r_2 \longrightarrow \infty, \qquad \frac{\partial \widehat{V}_{z0}}{\partial r_2} = 0. \tag{5.47}$$

In addition, a condition must be specified on $r_1 > 0$, $r_2 = 0$ which is compatible with (5.46) at the point $r_1 = r_2 = 0$. This is necessary because r_1 and r_2 are treated as independent variables. The reasonable choice is given by

$$\widehat{V}_{z0}(t, z, r_1, r_2 = 0) = -\overline{V}_{z0}(t, z). \tag{5.48}$$

Lastly, the condition at $z = 0$ in (5.29) is used.

The nonlinear term in (5.45), $\frac{1}{2}\partial(\widehat{V}_{z0})^2/\partial z$ is present in this study because the $O(M)$ boundary disturbance is larger than that used in earlier, basically linear studies (Flandro 1974, 1995*a*). Its presence suggests that wave steepening and other forms of instability may occur in the evolving flow field. If the imposed endwall disturbance is smaller, and/or axial variations are ignored, then a linear, viscous diffusion equation is derived.

The linear convection term in the diffusion equation (5.45) includes the axial convection effect, $V_{z0s}(\widehat{V}_{z0})_z$, retained somewhat arbitrarily by Flandro (1995*a*) in his analogue to (5.23). In the present multiple-scale formulation, the asymptotic analysis itself leads to the conclusion that the effect properly belongs in the higher-order diffusion equation, rather than in the lower-order inviscid axial momentum equation in (5.23).

6. Finite difference solutions for the nonlinear equation

A multiple-scale analysis is used in § 5 to develop a set of equations for the rotational axial velocity, $\widehat{V}_{z0}$. The lowest-order analysis leads to the first-order wave equation (5.23), which describes only the behaviour of $\widehat{V}_{z0}$ on the short radial scale, r_2. A higher-order analysis is necessary to resolve phenomena on the longer radial scale, r_1. This result is found in (5.45). When the full solution in (r_1, r_2)-space is evaluated along the intersection with the r_1–r_2 curve represented by the transformation in (5.2), one finds the desired physical solution in (r, z, t)-space, as shown schematically in figure 5.

For all the results that appear in the present work, the steady sidewall radial velocity, $V_{rw} = -1$, will be used for simplicity. The resulting integral transformation in (5.2) becomes

$$r_2 = -\frac{1}{M}\log\left(\tan\left(\pi(1 - r_1)^2/4\right)\right). \tag{6.1}$$

This relationship between r_1 and r_2 defines the curve along which the physical solution will be found. It is noted that $r_2 \to \infty$ as $r_1 \to 1$. This is in contrast to the linear transformation found in Staab *et al.* (1999) in which $r_1 = Mr_2$ is used. The solution in Staab *et al.* (1999) is restricted to $r_2 < Mr_1$ to ensure that the centreline is not crossed when the solution to (5.45) is found. In contrast, where the transformation in (5.2) is used there is no restriction on the domain of the solution in the present work.

The solution to (5.45)–(5.48) is found in three separate steps, denoted in figure 5, by the circled numbers:

1. Equation (5.23) is solved analytically along $r_1 = 0$, using the method of characteristics as described above, to find $\widehat{V}_{z0}(0, r_2, z, t)$. The solution is given in (5.46).

2. The solution $\widehat{V}_{z0}(0, r_2, z, t)$ is taken as the initial condition (or boundary at $r_1 = 0$)

https://doi.org/10.1017/S0022112000008454 Published online by Cambridge University Press

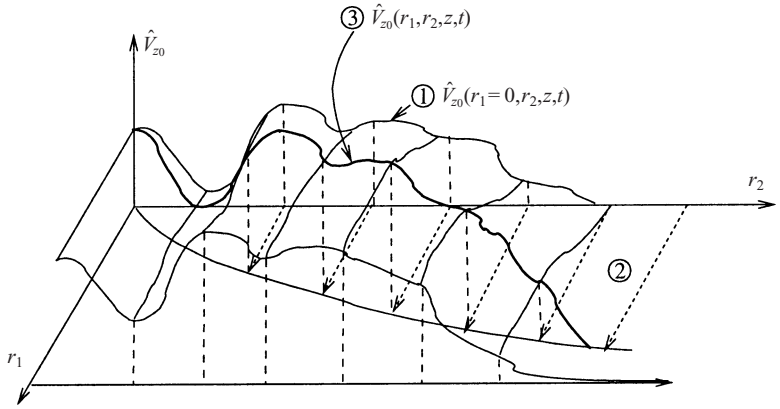


FIGURE 5. A graphical description of the solution development procedure. The circled numbers refer to the list in § 6. In the first step, the wave equation in (5.23) is solved along $r_1 = 0$. This is taken to be the boundary condition for (5.45) and the equation is solved in the domain $0 \leqslant r_2 \leqslant r_2^\star$ and $0 \leqslant r_1 \leqslant r_1^\star$, where $r_1^\star$ and $r_2^\star$ are explained in the text. Finally the full solution is evaluated along $r_2 = -\log(\tan(\pi(1-r_1)^2/4))/M$ to find the desired solution. The solid line in the (r_1, r_2)-plane is this curve.

for (5.45), which is solved subject to (5.29) and (5.47) to find the generalized solution $\widehat{V}_{z0}(r_1, r_2, z, t)$.

Although the r_2-domain of (5.23) and (5.45) is semi-infinite, the computational domain must be finite and the upper boundary, $r_2^\star$, is chosen to be sufficiently far beyond the wave front such that the condition in (5.47) is satisfied. The solution is also solved for $0 \leqslant r_1 \leqslant r_1^\star$ where $r_1^\star = \tan^{-1}(\mathrm{e}^{-Mr_2^\star})$, the solution of (6.1) for $r_1 = r_1^\star$ when $r_2 = r_2^\star$.

3. The solution $\widehat{V}_{z0}(r_1, r_2, z, t)$ at each z and t is evaluated along $r_2 = -\log(\tan(\pi(1-r_1)^2/4))/M$ to yield the desired physical solution in (r, z, t)-space.

It is noted that t is an implicit variable in (5.45) with the dependence driven by the 'initial' condition $\widehat{V}_{z0}(r_1 = 0, r_2, z, t)$ in (5.46). For a given value of t, the solution to the wave equation, (5.23), on $r_1 = 0$, penetrates a distance defined by the front, $\eta = 0$ in (5.32), and (5.45) describes the convection and diffusion effects of $\widehat{V}_{z0}$.

Equation (5.45) is solved via the method of lines, a numerical technique which employs a spatial discretization to reduce a PDE to a set of ordinary differential equations. The resulting set of ordinary differential equations is then solved using a standard ODE solver. A fourth-order approximation is used to discretize the r_2- and z-spatial derivatives in (5.45).

This discretization leads to a set of $N_{r_2}N_z$ coupled nonlinear ordinary differential equations, where N_z and N_{r_2} are the number of grid points chosen in the z- and r_2-directions respectively. The ODE set is solved using an adaptive fourth-order Runge–Kutta solver, which is a stable method for solving a set of ordinary differential equations that arise from the discretization of equations with both parabolic and hyperbolic terms.

At each value of the 'parameter' t, the integration is initiated with the initial conditions in (5.46), subject to the boundary conditions in (5.47). The spatial distribution of the solution with respect to r_2 evolves as the 'time-like' variable r_1 increases. Integration is carried out for $0 \leqslant r_1 \leqslant r_1^\star$. The physical solution $\widehat{V}_{z0}(z, t, r)$ is found from the intersection of the surface defined by $\widehat{V}_{z0}(z, t, r_1, r_2)$ and the curve relating r_1

https://doi.org/10.1017/S0022112000008454 Published online by Cambridge University Press

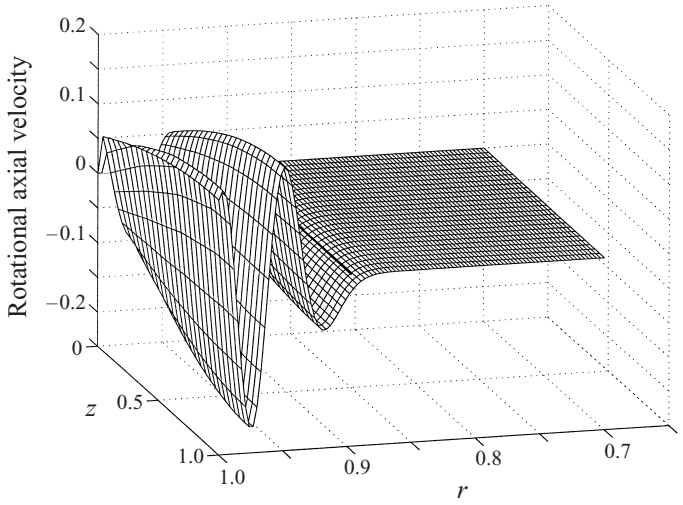


FIGURE 6. The axial velocity, $\widehat{V}_{z0}$ at $t = 10$ when $\omega = 1$ for the parameters $M = 0.01$, $Re = 3 \times 10^5$, and $\delta = 20$.

and r_2 in (6.1). In general this curve does not coincide with the computational grid points. Hence cubic spline interpolations in r_2 are employed at every chosen r_1 value to obtain the physical solution.

The accuracy of the results has been tested for $A = 0.1$, $M = 0.01$, $t = 20$, $Re = 3 \times 10^5$, $\delta = 20$. The number of grid points used is $N_z = 25$ and $N_z = 50$, and also $N_r = 50$ and $N_r = 100$. The test cases reveal that the difference between $N_r = 50$ and $N_r = 100$ is bounded by 10^{-3}. Results show that the difference between $N_z = 25$ and $N_z = 50$ is bounded by 4×10^{-3} away from $z = 0$, and 10^{-2} near $z = 0$. These bounds are sufficient for the Mach numbers considered here.

The larger errors near $z = 0$ are due to a boundary condition incompatibility at $z = 0$ and $r = 1$. On $z = 0$, $0 \leqslant r < 1$, the axial speed is prescribed by (2.12). In contrast, on $r = 1$, $z > 0$, the axial speed satisfies the no-slip condition. As a result, the corner point $z = 0$, $r = 1$ is the source of a singular solution to the partial differential equation that describes the flow. The local error is confined to a few grid points near $z = 0$, and has limited influence on the solution elsewhere.

7. Results

The results presented here have been found using the numerical method presented in the previous section. The number of radial and axial grid points for the method of lines shown above is $N_z = 25$ and N_{r_2} varies between 75 and 150 grids depending on the particular parameters. The former is sufficient to describe the relatively benign axial spatial gradients in the flow. All the results presented here use $A = 0.1$, $\delta = 20$ and $Re = 3 \times 10^5$ unless noted. Also the initial condition is obtained from (5.46) by using the first 40 Fourier modes.

7.1. *Properties of the axial rotational velocity*

The surface plots in figures 6–11 describe the radial and axial variation of the axial rotational velocity, $\widehat{V}_{z0}$ for various times and Mach numbers. These figures show the following general properties for $\widehat{V}_{z0}$:

https://doi.org/10.1017/S0022112000008454 Published online by Cambridge University Press

the inviscid front propagates from the sidewall at $t = 0$ toward the centreline as time evolves;

the speed of propagation is directly dependent on the Mach number;

the amplitude of the $\widehat{V}_{z0}$ spatial waves decays as they propagate toward the centreline;

the flow structure and the amount of decay of $\widehat{V}_{z0}$ depend on ω, the driving frequency;

the decay rate depends on both the Reynolds number and the axial convection.

Figure 6 is a surface plot of the axial rotational velocity $\widehat{V}_{z0}$ at $t = 10$ using $M = 0.01$, $\omega = 1$, $A = 0.1$, $Re = 3 \times 10^5$, and $\delta = 20$. The sidewall is located at $r = 1$ on the left of the plot, and the right endpoint is $r = 0.65$ (the centreline is not pictured). The endwall at $z = 0$ is in the background and the exit plane at $z = 1$ is located in the foreground of the plot. The boundary condition at the sidewall is the negative of the acoustic velocity in (5.18) to ensure that the total axial velocity satisfies the no-slip boundary condition.

At $t = 10$ two complete spatial waves are present and located between the sidewall and a viscous front located near $r = 0.89$. The *viscous front* is defined as the 0.001 contour of the amplitude of $\widehat{V}_{z0}$. The plot also shows the *undiffused vorticity front* near $r = 0.90$, a heavy black line. This front is defined by $\eta = 0$, or $r_{2e} = t$, where the subscript e denotes the edge. The solution of (6.1) for $r_e = 1 - r_1$ when $r_2 = Mt$ shows that the edge is located at the radial position

$$r_e(t) = \frac{2}{\sqrt{\pi}} \left(\tan^{-1}(\mathrm{e}^{-M\pi t})\right)^{1/2} \tag{7.1}$$

measured from the centreline. The inviscid front in figure 6 is invariant to axial location for spatially uniform sidewall injection. Its location compares very favourably with the diffused front location obtained from the complete numerical solution to (5.45), thus helping to verify the accuracy of the latter.

The theory in § 5.1 shows that vorticity is generated at the injection surface by the interaction of the acoustic pressure gradient with the injected fluid. To leading order, the vorticity is simply the radial gradient of the leading-order rotational axial velocity term as in (5.34). Hence the radial gradients of the waves present in figure 6 describe the vorticity waves.

The spatial waves in figure 6 have a wavelength of about 0.05 radial units. This is consistent with the second scale in the expansion in (5.2). The shorter scale captures phenomena on the order of the Mach number, $M = 0.01$ in this case. The precise spatial pattern is due to the pattern of oscillation in the acoustic pressure gradient as described above. The theory also shows that the vorticity generated at the sidewall is convected into the flow by the steady radial velocity. The results in figures 7 and 8 will show that the waves are convected toward the centreline.

Figure 7 shows the rotational axial velocity at $t = 20$. The two maximal peaks near $r = 1$ and $r = 0.95$ in figure 6 have moved to near $r = 0.9$ and $r = 0.85$. The inviscid front at $r_e = 0.79$ is located about twice as far from the sidewall as in the previous plot. The location of both the peaks and the inviscid front is consistent with the distance travelled by a fluid particle during a time interval of 10 units. This distance, denoted by Δr, is approximated near the sidewall by

$$\Delta r = \frac{\Delta r'}{R'} = \frac{\Delta t' V'_{r0}}{R'} = \frac{t'_a V'_{r0}}{R'} \Delta t = \frac{L' V'_{r0}}{C'_0 R'} \Delta t = M \Delta t,$$

https://doi.org/10.1017/S0022112000008454 Published online by Cambridge University Press

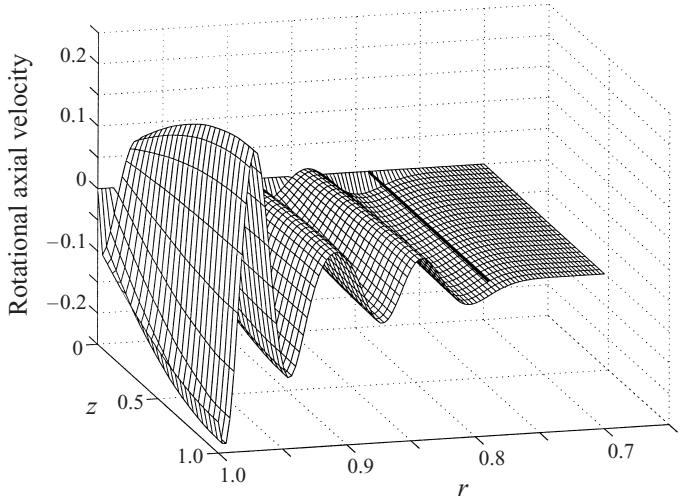


FIGURE 7. The axial velocity, $\widehat{V}_{z0}$ at $t = 20$ when $\omega = 1$ for the parameters $M = 0.01$, $Re = 3 \times 10^5$, and $\delta = 20$.

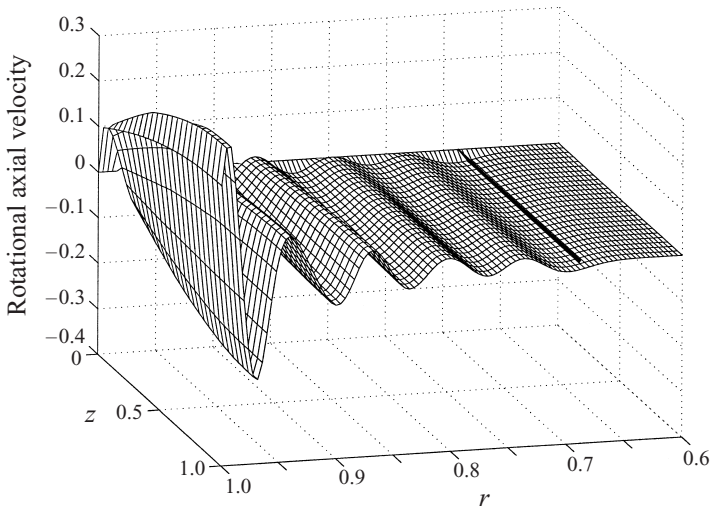


FIGURE 8. The axial velocity, $\widehat{V}_{z0}$ at $t = 30$ when $\omega = 1$ for the parameters $M = 0.01$, $Re = 3 \times 10^5$, and $\delta = 20$.

where the definitions in (2.6) are used and $\Delta r'$ and $\Delta t'$ are dimensional distance and time intervals respectively. The distance travelled by a fluid particle between $t = 10$ and $t = 20$ with a Mach number of $M = 0.01$ is 0.1 radial units.

Figure 7 also shows the effects of viscous diffusion and axial convection on $\widehat{V}_{z0}$. The amplitude of the two peaks in figure 6 have decreased substantially during the time interval from $t = 10$ to $t = 20$. The viscous front at $t = 20$ has diffused further past the inviscid front location than for $t = 10$ in figure 6. The difference can be explained in terms of the accumulated effect of viscous diffusion and axial convection as explained later.

https://doi.org/10.1017/S0022112000008454 Published online by Cambridge University Press

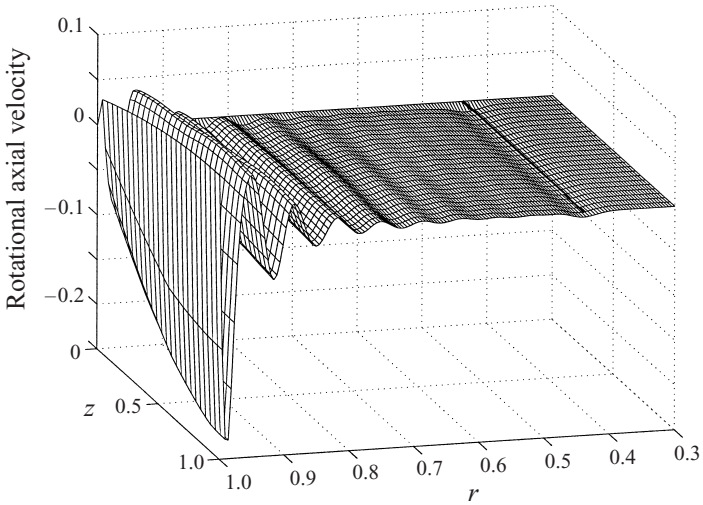


FIGURE 9. The axial velocity, $\widehat{V}_{z0}$ at $t = 60$ when $\omega = 1$ for the parameters $M = 0.01$, $Re = 3 \times 10^5$, and $\delta = 20$.

More spatial waves are seen in figure 8 at $t = 30$. The undiffused velocity front, shown by the heavy black line, has moved to $r = 0.68$. Here again, one sees a decrease in the amplitude of $\widehat{V}_{z0}$ in the radial direction.

Figure 9 shows $\widehat{V}_{z0}$ at $t = 60$. The inviscid front is now located at $r_e = 0.44$. The surface plot shows that the amplitude of the axial rotational velocity is less than 10^{-3} for radial locations less than 0.7.

The wave near $r = 0.45$ is larger in amplitude that the waves nearest it. Although this is not well understood, it is not a numerical artifact and has been seen in the model problem in the Appendix. In this model problem, the first wave decays at a slower rate than the waves behind it.

Figure 10 shows $\widehat{V}_{z0}$, at $t = 50$ for $\omega = 1.4$ and $Re = 3 \times 10^6$. A near-resonant frequency is chosen to show the possibility of beats in the flow structure. The acoustic field for $\omega = 1.4$ is seen in figure 2(*b*). The Reynolds number is 10 times higher than in the previous figures to minimize viscous diffusion and show more structure.

Staab *et al.* (1999) have performed analysis on (5.45) with the convection terms dropped. They show that this model can be solved analytically and that

$$\widehat{V}_{z0} \sim \left(\tan\frac{\pi r^2}{4}\right)^{B\omega^2/Re}, \qquad B = \frac{2\delta^2}{\pi(1+A)^2M^2}. \tag{7.2}$$

One can use this model solution to learn how the parameter values affect solution decay near the centreline $r = 0$. As the centreline is approached, the decay of $\widehat{V}_{z0}$ depends on the ratio ω^2/Re. For a given Re, the axial velocity will decay almost twice as fast for $\omega = 1.4$ compared to the $\omega = 1$ case. The decay rate can be reduced by an appropriate increase in the Reynolds number.

Figure 11 shows a surface plot of $\widehat{V}_{z0}$ at $t = 20$ when $\omega = 1$ for a larger Mach number, $M = 0.02$, than in the previous figures. In comparison to the result in figure 7, for $M = 0.01$ and $t = 20$, the waves have travelled about twice as far into the flow field for the same time period due to enhanced radial convection. This can be

https://doi.org/10.1017/S0022112000008454 Published online by Cambridge University Press

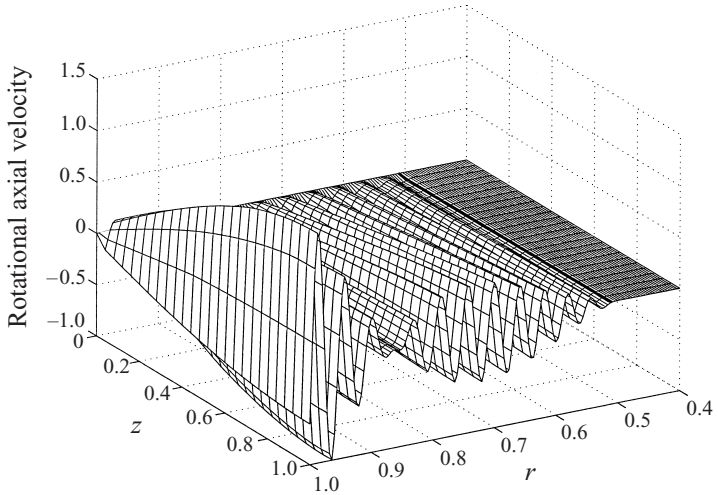


FIGURE 10. The axial velocity, $\widehat{V}_{z0}$ at $t = 50$ when $\omega = 1.4$ for the parameters $M = 0.01$, $Re = 3 \times 10^6$, and $\delta = 20$.

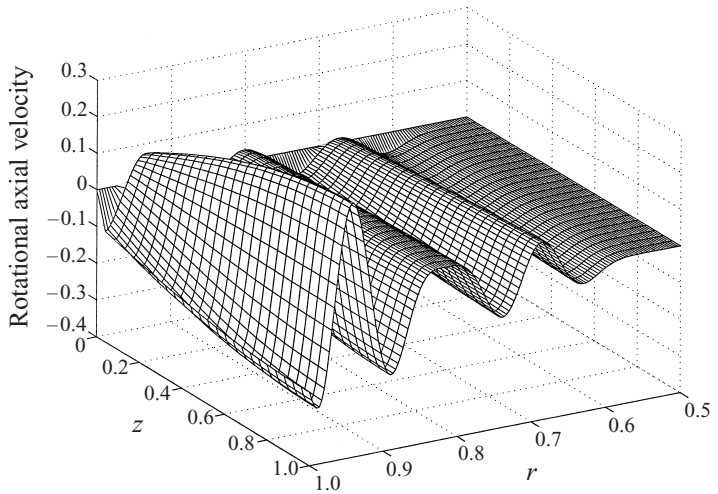


FIGURE 11. The axial velocity, $\widehat{V}_{z0}$ at $t = 20$ when $\omega = 1$ for the parameters $M = 0.02$, $Re = 3 \times 10^5$, and $\delta = 20$.

explained by the relationship,

$$M = \frac{V'_{r0} L'}{C'_0 R'}$$

which shows that an increase in V'_{r0} increases the Mach number.

Examination of the axial rotational velocity along the sidewall in figures 6–11 shows that vorticity, evident from the large radial gradient on the sidewall, is produced at $r = 1$. The surface plot of the unsteady vorticity distribution in figure 12 shows the axial and radial distribution, where the unsteady vorticity is defined in (5.34).

The amplitude of the vorticity on the sidewall is about 30, which is consistent with the $O(1/M)$ magnitude in the result in (5.34). The result also shows that vorticity is in the region $0.68 \leqslant r \leqslant 1$. Similar results taken at larger times reveal that vorticity

https://doi.org/10.1017/S0022112000008454 Published online by Cambridge University Press

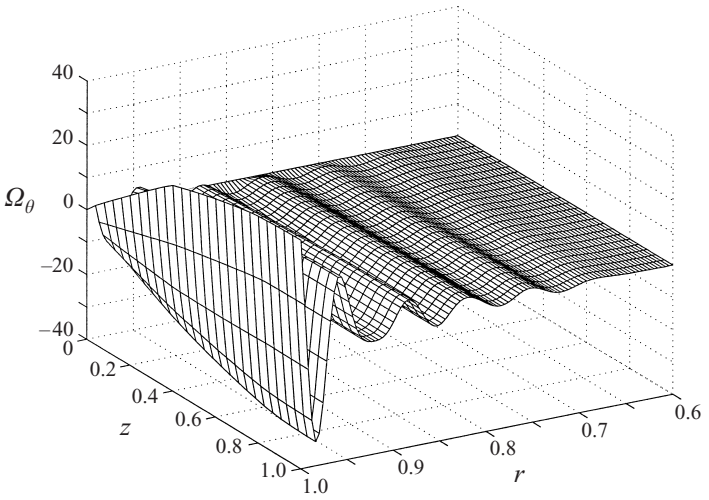


FIGURE 12. The unsteady vorticity, at $t = 30$ when $\omega = 1$ for the parameters $M = 0.01$, $Re = 3 \times 10^5$, and $\delta = 20$.

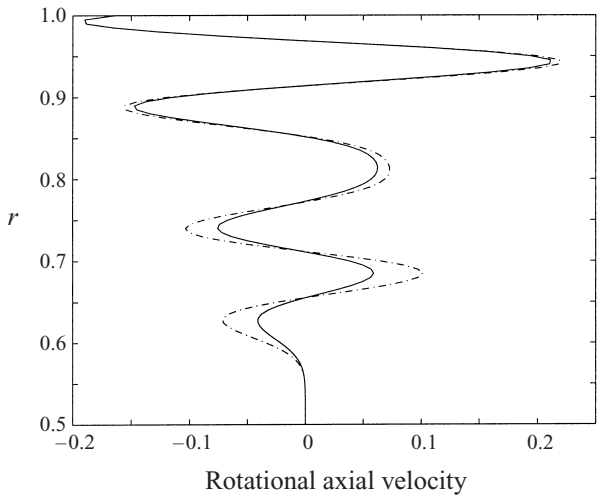


FIGURE 13. Comparison of the rotational axial velocity, $\widehat{V}_{z0}$, at $A = 0.1$, $M = 0.02$, $Re = 3 \times 10^5$ and $z = 0.5$. The solid line is the solution to (5.45), and the dashed line is the solution to (5.45) with the nonlinear term, $\partial \widehat{V}_{z0}^2/\partial z$ reduced by a factor of 10^{-5}.

exists between the sidewall and the inviscid front defined earlier. The amplitude of the vorticity waves is also affected by the boundary driving frequency and the Reynolds number in the same manner as the axial rotational velocity.

Figure 13 shows the effect of axial convection on $\widehat{V}_{z0}$. The solid curve shows the complete solution to (5.45) while the dashed-dot curve shows the solution to (5.45) when the axial convection terms are reduced by 10^{-5}. The result, given at $z = 0.5$, for $t = 20$, $Re = 3 \times 10^5$, $\delta = 20$, and $M = 0.02$, shows that axial convection plays an important role in decreasing the magnitude of $\widehat{V}_{z0}$ and hence the unsteady vorticity.

The conclusion about the effect of axial convection obtained by the numerical result is supported by the results of a model problem of Staab *et al.* (1999). They examine

https://doi.org/10.1017/S0022112000008454 Published online by Cambridge University Press

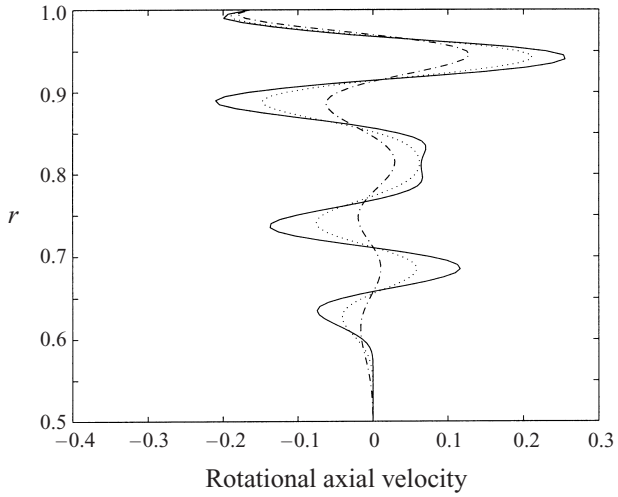


FIGURE 14. A plot of three rotational axial profiles at the Reynolds numbers, $Re = 10^6$ (solid line), $Re = 3 \times 10^5$ (dotted line), and $Re = 10^5$ (dash-dot line). The result shows as expected that the higher the Reynolds number, that less diffusion occurs. The remaining parameters are $\delta = 20$, $M = 0.01$, $z = 0.5$.

(5.45) with the diffusion term dropped and show analytically that the presence of axial convection decreases the magnitude of the solution to the model problem.

The effect of the Reynolds number on $\widehat{V}_{z0}$ is considered in figure 14. The solid curve is for $Re = 10^6$, the dotted curve for $Re = 3 \times 10^5$, and the dash-dot curve for $Re = 10^5$. The plot is taken at $z = 0.5$ for $t = 20$, $M = 0.02$, $\delta = 20$, $A = 0.1$ and $\omega = 1$. The results show that the amplitude of each of the peaks is reduced by a decrease in Reynolds number associated with a larger viscous effect. This is consistent with the results of the model problem in (7.2), which shows an increase in the decay rate of $\widehat{V}_{z0}$ with a decrease in Reynolds number.

The two sets of peaks for the solid curve between $r = 0.78$ and $r = 0.8$ are due to the shape of the acoustic field. This same pattern can be seen in figure 2 near $t = 12$ for $\omega = 1$. The large Reynolds number for the solid curve results in very little diffusion. For the smaller Reynolds number cases (the dashed-dot and dotted curves), diffusive effects have smoothed the two peaks into one peak.

7.2. *The complete velocity field*

The previous section discussed the dynamics of the rotational axial velocity, $\widehat{V}_{z0}$, and its dependence on the flow parameters. The results presented in figures 15 and 16 show the complete leading-order velocity flow field.

Figure 15 shows a series of plots of axial profiles at $t = 5, 10, 15$, and 20, at the axial locations, $z = 0.24, 0.48$, and 0.72. The remaining parameters are $M = 0.01$, $A = 0.2$, $Re = 3 \times 10^5$, $\delta = 20$, and $\omega = 1$.

All the plots show that vorticity is generated along the sidewall. This is evident from the large radial gradient of the axial velocity at $r = 1$. The four plots show that roughly 1, 2, 3, and 4 waves have been generated and convected into the flow field for increasing time. The plots also show that the axial velocity magnitude increases in the downstream direction. This is mainly due to the steady axial velocity in (3.6).

The results for $t = 5$ and $t = 10$ show that there is a region of negative axial velocity near the sidewall, while at $t = 15$ and $t = 20$, the flow near the sidewall is

https://doi.org/10.1017/S0022112000008454 Published online by Cambridge University Press

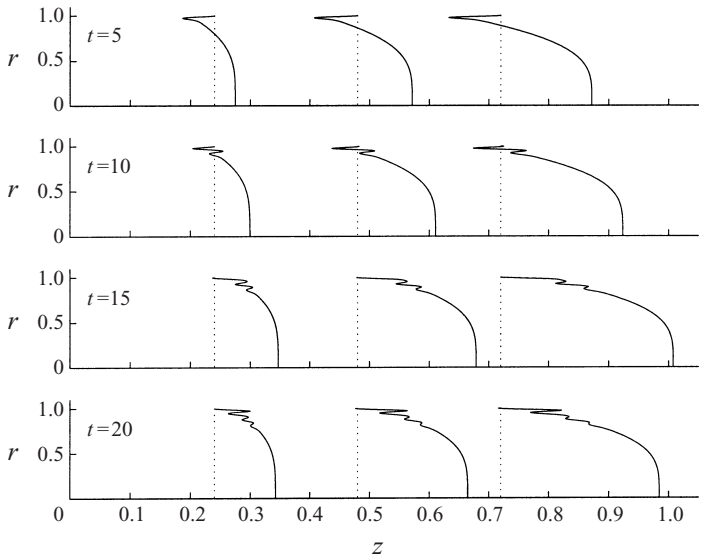


FIGURE 15. A plot of a series of axial profiles at $t = 5, 10, 15$, and 20, at the axial locations $z = 0.24$, 0.48, and 0.72. The plots show that the vorticity generated along the sidewall propagates into the flow field and diffuses. The length scale of vorticity is on the order of the Mach number, 0.01 in this case. The velocity at the centreline is a combination of the acoustic and steady fields. The difference in centreline velocities over time is due to the acoustics, and the difference in velocities at axial location is mainly due to the steady field.

positive. This is due to the fact that the acoustic axial velocity is negative for the first two times and positive for the second two times. This can be seen in figure 2 when $\omega = 1$. The flow field away from the sidewall is dominated by the steady axial velocity which is always positive. Also, the magnitude of the rotational velocity is small away from the sidewall due to the axial convection and radial diffusive effects discussed previously.

One may observe that the vorticity generated along the sidewall propagates into the flow field and diffuses. The length scale of vorticity seen in this result is consistent with the analysis, which shows that small-scale phenomena are on the order of the Mach number, 0.01 in this case. The velocity at the centreline is a combination of the acoustic and steady field. The difference in centreline velocities over time is due to the acoustics, and the variation in velocity with axial location is due mainly to the axial variation of the steady field.

Five direction field plots appear in figure 16 near the sidewall. The domain for each plot is $0.85 \leqslant r \leqslant 1$ and $0 \leqslant z \leqslant 1$, with the remaining parameters $\omega = 1$, $Re = 3 \times 10^6$, $M = 0.01$, $A = 0.4$, and $\delta = 20$. The direction field is the total radial and axial velocities, with the radial velocity multiplied by 0.2 to emphasize the axial velocities. All of the vectors have been normalized to emphasize direction of flow and not speed. The plots show that there is mainly positive axial flow at $t = 0$, 2, and 8, while for the remaining times, negative axial velocity is present. This is similar to the result in figure 15.

The result for $t = 0$ consists only of the steady velocity field. At $t > 0$, the velocity at the endwall is turned on and the blowing of mass is evident at $z = 0$ for all of the plots. Evidence of organized vorticity can be seen at $t = 4$ on the right-hand side of the plot with an instantaneous counterclockwise motion of the fluid. Smaller-scale vorticity (hence larger in magnitude) is seen in the $t = 6$ and $t = 10$ plots.

https://doi.org/10.1017/S0022112000008454 Published online by Cambridge University Press

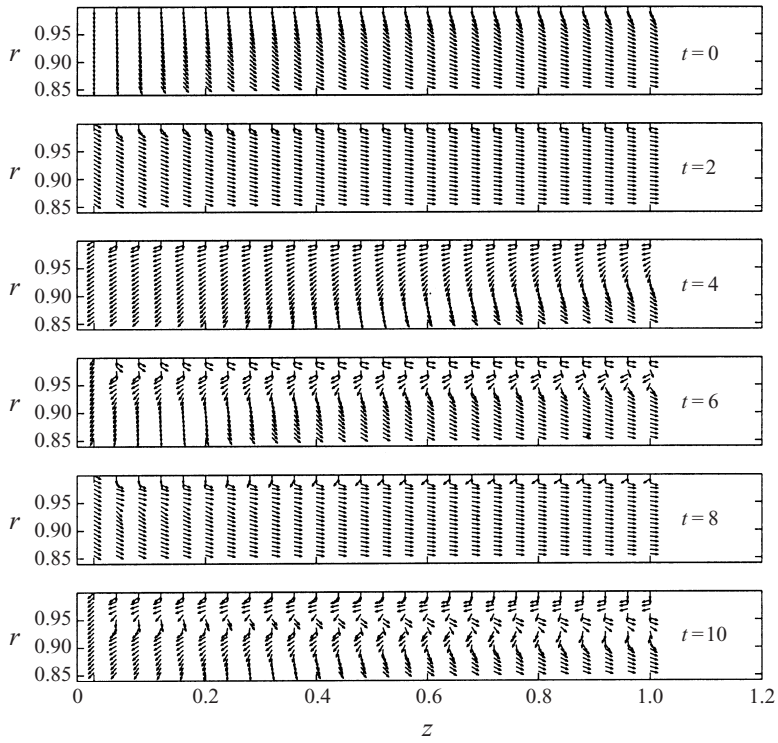


FIGURE 16. A vector field plot of the velocity near the sidewall, $r = 1$. The plot shows that a region of backwards flow (toward the endwall) exists for a thin layer near the wall. The acoustic field drives the fluid exiting the sidewall toward the endwall.

8. Energetics of the internal flow

The prescribed axial speed disturbance imposed on the endwall in (2.12) causes transient work to be done on the flow system. Acoustic disturbances originating at the end distribute the energy into the flow field. Simultaneously, energy is transferred from the acoustic field into the rotational flow field as vorticity is generated at the sidewall and redistributed in the internal flow. This partition of transient energy between the acoustic and rotational flows is of interest in understanding the flow dynamics. It has been considered in terms of the concept of 'flow turning' used in the solid rocket motor stability literature (Flandro 1995*b*, for example).

The endwall work input rate can be written in non-dimensional form as

$$W_e(t) = MA \int_0^t P(0,t) \sin \omega t \mathrm{d}t \tag{8.1}$$

where $P(0,t)$ is obtained from (5.1) and (5.19) to $O(M)$. It follows that

$$\frac{W_e(t)}{MA} = \frac{1}{\omega}(1 - \cos(\omega t)) + A\omega M \sum_{n=1}^{\infty} \frac{1}{(\lambda_n^2 - \omega^2)} \times \left\{ \frac{1 - \cos(2\omega t)}{2\omega} - \left[\frac{(1 - \cos(\omega + \lambda_n)t)}{\omega + \lambda_n} + \frac{(1 - \cos(\omega - \lambda_n)t)}{\omega - \lambda_n} \right] \right\}, \tag{8.2}$$

https://doi.org/10.1017/S0022112000008454 Published online by Cambridge University Press

describes the time-history of the work input to $O(M)$. The long-time average,

$$\bar{W}_e = \lim_{T\to\infty} \frac{1}{T} \int_0^T W_e \mathrm{d}t = MA \left[\frac{1}{\omega} + MA \sum_{n=1}^{\infty} \frac{(3\omega^2 + \lambda_n^2)}{(\lambda_n^2 - \omega^2)^2} \right], \tag{8.3}$$

is positive definite and the series converges rapidly. This added energy must now be partitioned into the acoustic and rotational fields.

One may write the non-dimensional total energy per unit mass of a fluid particle in the form

$$\begin{aligned} E &= E' \Big/ \left(\frac{C_0'^2}{\gamma(\gamma-1)} \right) \\ &= \left\{ 1 + \frac{\gamma(\gamma-1)}{2} M^2 \left(V_{z0s}^2 + \frac{1}{\delta^2} V_{r0s}^2 \right) \right\} + M\widetilde{T}_0 \\ &\quad + M^2 \left\{ \widetilde{T}_1 + \frac{\gamma(\gamma-1)}{2} \left(2V_{z0s}(\overline{V}_{z0} + \widehat{V}_{z0}) + (\overline{V}_{z0} + \widehat{V}_{z0})^2 + O\left(M, \frac{1}{\delta^2}\right) \right] \right\}. \end{aligned} \tag{8.4}$$

The first two terms in curly brackets represent steady flow energy, while the third includes both acoustic and rotational components defined in (5.9). The $O(M)\widetilde{T}_0$ term arises directly from the endwall disturbance and is larger than the biggest kinetic energy term of $O(M^2)$ in this low Mach number flow. Energy in this thermal term and the analogous $\widetilde{T}_1$-term cannot be evaluated until solutions are developed in a future paper. However, it is clear from the present formulation that a thermal accommodation layer will be present in order to satisfy an imposed wall temperature boundary condition (i.e. (2.9)), like those studied by Roh & Yang (1995).

The largest component of the *unsteady* kinetic energy, Λ, can be written in the non-dimensional form:

$$\frac{\Lambda}{\gamma(\gamma-1)M^2} = V_{z0s}(\overline{V}_{z0} + \widehat{V}_{z0}) + \tfrac{1}{2}(\overline{V}_{z0} + \widehat{V}_{z0})^2, \tag{8.5}$$

which includes both acoustic and rotational flow contributions. Equations (5.12) and (5.23) can then be employed to derive an expression for the rate of change of Λ for fluid particles entering the cylinder from the sidewall:

$$\frac{\partial \Lambda}{\partial t} + \frac{\partial \Lambda}{\partial r_2} = -M^2(\gamma-1)(V_{z0s} + \overline{V}_{z0} + \widehat{V}_{z0}) \frac{\partial P_0}{\partial z}. \tag{8.6}$$

Then a variable transformation employing $\eta = t - r_2$ can be used to write a Lagrangian equation for $\Lambda(t, \eta, r_1, z)$:

$$\left. \frac{\partial \Lambda}{\partial t} \right|_{\eta} = -M^2(\gamma-1)(V_{z0s} + \overline{V}_{z0} + \widehat{V}_{z0}) \frac{\partial P_0}{\partial z}. \tag{8.7}$$

It follows that on a constant-η line the kinetic energy is altered by an interaction between the complete $O(1)$ axial velocity and the axial gradient of the acoustic pressure. One should note that the rotational field itself ($\widehat{V}_{z0}$) affects the change in Λ.

One can integrate (8.7) by following a convecting fluid particle on a given η line from the time it exits the sidewall ($t = \eta$) to any larger value of time. It follows that

$$\Lambda = \Lambda_0 + \gamma(\gamma-1)M^2(\overline{V}_{z0}(t,z) - \overline{V}_{z0}(\eta,z)) \left[V_{z0s} + \frac{\overline{V}_{z0}(t,z) + \overline{V}_{z0}(\eta,z)}{2} + \widehat{V}_{z0} \right] \tag{8.8}$$

where $\Lambda_0 \equiv \Lambda(\eta, \eta, r_1, z)$ is obtained from (8.5). Equation (8.8) describes the evolution

https://doi.org/10.1017/S0022112000008454 Published online by Cambridge University Press

of the fluid particle kinetic energy on a given η line. It is perhaps more illustrative to find the time-average of (8.8), in order to integrate away harmonic function variations. The result is that

$$\lim_{T\to\infty}\frac{1}{T}\int_0^T \Lambda \mathrm{d}t = \gamma(\gamma-1)M^2\left\{\lim_{T\to\infty}\frac{1}{T}\int_\eta^T \frac{\overline{V}_{z0}^2}{2}\mathrm{d}t + V_{z0s}\widehat{V}_{z0} + \frac{\widehat{V}_{z0}^2}{2}\right\} \tag{8.9}$$

where the value of Λ_0 has been used.

The first term on the right-hand side of (8.9) describes the average acoustic kinetic energy and is positive definite. One can observe a form of long-time kinetic energy partitioning between the acoustic and rotational fields.

It is interesting to note that the long-time average of (8.7) on a constant-η line vanishes:

$$\lim_{T\to\infty}\frac{1}{T}\int_\eta^T \left.\frac{\partial \Lambda}{\partial t}\right|_\eta \mathrm{d}t = 0. \tag{8.10}$$

This result and (8.7) imply that the kinetic energy increases in some intervals and decreases in others, with the average value on a constant-η line given by (8.9).

These issues are worthy of additional consideration in the future because the flow is fundamentally rotational in character. As a result, traditional acoustic intensity arguments cannot be employed to elucidate the fundamental energy partitioning processes.

9. Conclusions

Systematic asymptotic methods have been employed to formulate an initial-boundary-value model for co-existing acoustic and rotational flow fields in a long narrow cylinder. Boundary-driven axial planar acoustic waves interact with an inviscid weakly rotational injection-induced steady flow to produce intense time-dependent vorticity at the sidewall of the cylinder. For appropriate ranges of Reynolds number, Mach number, and frequency, the intense vorticity penetrates far into the chamber due to convection by the steady radial velocity field. The amplitude and distribution of the vorticity is impacted by weak viscous and nonlinear effects.

Results for non-resonant frequency values show that the spatial wave amplitudes in the rotational axial velocity decline monotonically as the centreline is approached. In contrast, near-resonant frequencies produce non-monotonic 'bursts' of spatial waves as a response to beats in the time variation of the axial gradient of the acoustic pressure.

Numerical experiments based on the equations derived have been used to demonstrate that nonlinear axial convection is a source of spatial wave amplitude decline in addition to the more familiar effect of viscous diffusion.

The details of the spatial wave structure are quantitatively sensitive to the axial flow Reynolds number. An increase in Re from 10^5 to 10^6 causes new details to appear.

The complete axial velocity variations show narrow localized regions of reverse flow. One can observe long thin vortices stretched out along the axial direction for this case of uniform wall injection.

It is also demonstrated that there are parameter ranges of Mach number (as it relates to injection rate), driving frequency and Reynolds number for which vorticity is really confined to weakly viscous acoustic boundary layers, thin compared to

https://doi.org/10.1017/S0022112000008454 Published online by Cambridge University Press

the radius of the cylinder, but larger than those discussed by Flandro (1974), and Baum & Levine (1987). These structures can appear for relatively small injection rates, relatively high driving frequency and low Reynolds numbers, so that viscous damping of the vorticity amplitude is profound. Then, the cylinder core will contain the relatively weak vorticity of the steady Culick (1966) solution and irrotational acoustic waves driven by the boundary forcing.

There is now a considerable body of evidence in support of the presence of an unsteady vorticity distribution within an appropriately high Reynolds number wall-injected flow in a cylinder. The experiments of Brown *et al.* (1986*a*, *b*), the small-disturbance linear stability modelling of Flandro (1995*a*, *b*) as well as Majdalani & Van Moorhem (1997, 1998), the computational solutions of Vuillot & Avalon (1991), Smith *et al.* (1993), and that of Kirkkopru *et al.* (1995, 1996, 1999) as well as the current work show unequivocally that unsteady vorticity is generated at the cylindrical surface and is convected away by the injected fluid. The core of the cylinder is free of intense unsteady vorticity only during the very early phases of the transient process, prior to the arrival of a well-defined unsteady vorticity front.

Unlike the recent work of Flandro (1995*a*, *b*) and that of Majdalani & Van Moorhem (1997, 1998), which employs quasi-steady linear small-disturbance stability theory for explaining the observed presence of rotational flow throughout the cylinder, we have formulated an initial-boundary-value theory for a weakly nonlinear and viscous flow process. A multiple-length-scale analysis, which is essential in forming a rational mathematical model, is used to demonstrate to first order that the vorticity is generated at the surface by a fundamentally inviscid interaction between the acoustic pressure axial gradient and the injected fluid at the wall, and is convected away by a steady radial velocity field. Then, a higher-order theory is used to prove that the basic vorticity is non-linearized in the axial direction and viscously diffused on a small radial length scale. The latter result demonstrates that the weak viscosity is pervasive, although smaller in magnitude than the driving effect of the axial pressure gradient, and confirms the conjecture of Hegde *et al.* (1986). These results are a generalization of those by Flandro (1995*b*) and Majdalani & Van Moorhem (1997, 1998).

The amplitude of the transient vorticity distributions described by Kirkkopru *et al.* (1995), and in the present work are $O(M^{-1})$ larger than that of the Culick (1966) steady solution. It follows that there will be a relatively large transient axial shear stress on the cylinder surface, which can be calculated from equation (5.33), particularly for smaller M values. This result has important consequences for applications of the theory to solid rocket motor combustion.

One can speculate that the large transient shear stresses will impact the burning rate of a propellant which is the source of the 'injected' fluid used in the present model. Perhaps there is a direct relationship between the effect of surface shear stress transients, predicted in the present work, and erosive burning concepts used in the solid rocket engineering literature (Williams 1985).

The linear acoustic pressure field in our theory is found independently of any vorticity distribution present in the cylinder. It is mathematically decoupled from the vorticity subsequently generated by the inviscid interaction between the axial pressure gradient and the fluid injected at the wall. As a result, the pressure field is determined from an irrotational formulation, using a homogeneous wave equation with non-homogeneous boundary conditions. The solution, composed of a forced (Helmholtz) response and eigenfunctions (travelling waves) resembles what one measures in rocket motor models. However, the total axial velocity response arises from the co-existing acoustic and rotational flow fields of equal magnitude. The latter includes the 'shear

https://doi.org/10.1017/S0022112000008454 Published online by Cambridge University Press

waves' or vorticity distribution. The associated radial gradient cannot be predicted from acoustic stability theory.

The conceptual approach used here has been extended by Staab *et al.* (1999) to disturbances driven by sidewall injection transients, rather than those applied at the closed endwall (Zhao & Kassoy 1994). The former type of disturbance emulates the effects of propellant burning rate variations in solid rocket motors. These methods have also proved effective for studying three-dimensional flow responses to non-axisymmetric boundary disturbances, Kassoy *et al.* (1997), Staab & Kassoy (1996), and Staab (1998).

Appendix. Solution to a related model problem

The nonlinear coupled system in (5.45) is sufficiently complex to require a computational solution. In order to develop an effective numerical approach, it is desirable to consider the solution to an elementary model problem with related properties. A simple Fisher equation (Fisher 1936) with appropriate periodic initial and boundary conditions can be used:

$$\frac{\partial U}{\partial z} = \frac{\partial^2 U}{\partial y^2} + \nu U^2, \tag{A 1}$$

initial condition:

$$U(0,y) = \begin{cases} -\sin(t-y) & \text{for} \quad 0 \leqslant y \leqslant t \\ 0 & \text{for} \quad y > t, \end{cases} \tag{A 2}$$

boundary condition:

$$U(z,0) = -\sin(t). \tag{A 3}$$

When the parameter t is increased, the non-zero portion of the initial condition is spread farther into the y-domain. In the spirit of (5.45), the multiple-scale independent variables are related by $y = \Omega^2 z$ and $\Omega \gg 1$.

An analytical solution for linear diffusion ($\nu = 0$) is constructed for the odd extension of (A 1)–(A 3) for the domain $0 < y < \infty$:

$$U(y,z) = -\frac{1}{2\sqrt{\pi z}} \int_0^t \sin(t-y') \left[\mathrm{e}^{-(y-y')^2/4z} - \mathrm{e}^{-(y+y')^2/4z} \right] \mathrm{d}y' \\ -\frac{y}{2\sqrt{\pi}} \int_0^z \frac{\sin t}{(z-z')^{3/2}} \mathrm{e}^{-y^2/4(z-z')} \, \mathrm{d}z', \quad y > 0. \tag{A 4}$$

A quasi-steady solution form $U(y,z) = -\sin(t-y)\mathrm{e}^{-z}$ can be recovered by taking the limits $(y \pm t)/2\sqrt{t}) \to \pm\infty$ simultaneously. Physically, this means that the solution has a quasi-steady form at specific value of t if y lies between $y = 0$ and the inner edge of a diffusive boundary layer centred at $y = t$ which is needed to smooth the discontinuous slope of the initial condition (A 2) and (A 3) at that location. Inside the diffusive layer, the solution is given by the full form of (A 1). The diffusive layer thickness is $\delta \sim O(\sqrt{z}/\Omega^2)$.

The solution to (A 1)–(A 4) along the locus $y = \Omega^2 z$, for $\nu = 1$ and $\Omega^2 \approx 66$, has been found from a computational analysis based on a method of lines implementation similar to that described in § 6. The solid line in figure 17 describes the linear solution when $t = 100$ obtained from (A 1). An analogous numerical result ($\nu = 0$) is indistinguishable from the analytical solution on the scale of the graph, thus verifying the numerical code. The linear solution shows regular, nearly harmonic,

https://doi.org/10.1017/S0022112000008454 Published online by Cambridge University Press

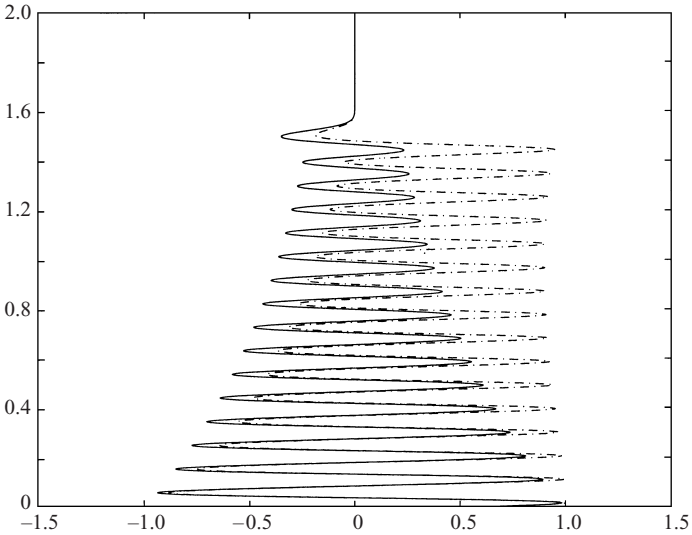


FIGURE 17. Solution U vs. z for the nonlinear model problem on the locus $y = \Omega^2 z$ with $\Omega^2 \approx 66$ for $v = 1$ (dashed-dot curve) and $v = 0$ (solid line).

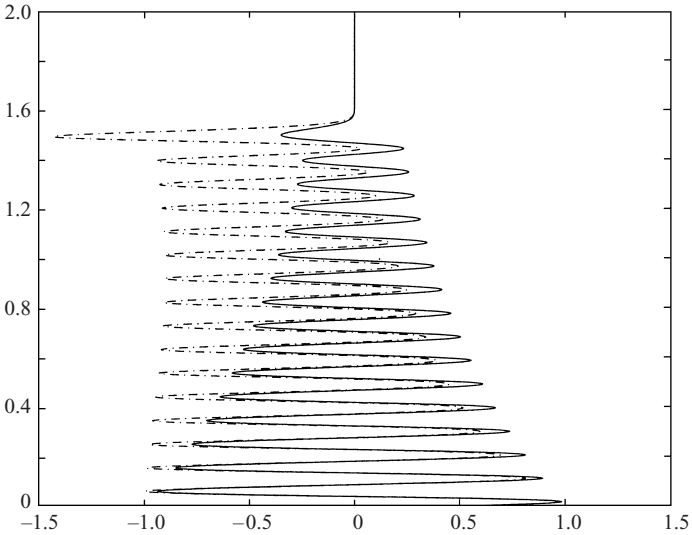


FIGURE 18. Solution U vs. z for the nonlinear model problem on the locus $y = \Omega^2 z$ with $\Omega^2 \approx 66$ for $v = -1$ (dashed-dot curve) and $v = 0$ (solid curve).

spatial oscillations that decay until the diffusive layer is reached near $z \approx 1.5$. There the solution makes a rapid transition to a vanishingly small value for $z > 1.5$. The solution also shows that the peak with location near $z \approx 1.5$ is larger in magnitude than the nearest peak ($z \approx 1.4$). This has been seen in the full numerical solution in figure 9.

In comparison the dashed-dot line represents the nonlinear numerical solution for $v = 1$. The frequency is nearly identical to the linear solution. However, the drift of the solution toward large positive value of U is due to the positive definite source effect of vU^2. Again the deviation from the pattern of oscillations near $z \approx 1.5$ is associated

https://doi.org/10.1017/S0022112000008454 Published online by Cambridge University Press

with the diffusive layer behaviour. Given the parameters used in the calculation, the diffusive layer thickness with respect to the z-coordinate is about 0.1. The analogous results for $v = -1$, corresponding to a nonlinear sink, are given in figure 18. There is no expectation of symmetry.

The basic properties of the model problem solution can be used to develop an effective numerical method for the solution of (5.45).

REFERENCES

Avalon, G., Casalis, G. & Grifford, J. 1998 Flow instabilities and acoustic resonance of channels with wall injection. *AIAA Paper* 98-3218.

Balakrishnan, G., Liñán, A. & Williams, F. 1991 Compressibility effects in thin channels with injection. *AIAA J.* **29**, 2149–2154.

Baum, J. D. 1989 Investigation of flow turning phenomenon. *AIAA Paper* 89-0297.

Baum, J. D. 1990 Energy exchange mechanisms between the mean and acoustic fields in a simulated rocket combustor. AFOSR Contractors Meeting (personal communication).

Baum, J. D. & Levine, J. N. 1987 Numerical investigation of acoustic refraction. *AIAA J.* **25**, 1577–1586.

Brown, R. S., Blackner, A. M., Willoughby, A. M. & Dunlap, R. 1986*a* Coupling between acoustic velocity oscillations and solid propellant combustion. *J. Propulsion Power* **2**, 428–437.

Brown, R. S., Blackner, A. M., Willoughby, P. G. & Dunlap, R. 1986*b* Coupling between velocity oscillations and solid propellant combustion. *AIAA Paper* 86-0531.

Brown, R. S. & Shaeffer, C. W. 1992 Oscillatory internal flow field studies. AFOSR Contractors Meeting in Propulsion, La Jolla, CA (personal communication).

Casalis, G., Avalon, G. & Pineau, J.-P. 1998 Spatial instability of planar channel flow with fluid injection through porous walls. *Phys. Fluids* **10**, 2558–2568.

Chen, T., Hegde, U. & Zinn, B. 1990 Driving of axial acoustic fields by sidewall stabilized diffusion flames. *AIAA Paper* 90-0037.

Cole, J. D. & Aroesty, J. 1968 The blowhard problem-inviscid flows with surface injection. *Intl J. Heat Mass Transfer* **11**, 1167–1183.

Cole, J. D. & Kevorkian, J. 1996 *Multiple Scale and Singular Perturbation Methods*. Springer.

Culick, F. E. C. 1966 Rotational axisymmetric mean flow and damping of acoustic waves in a solid propellant. *AIAA J.* **4**, 1462–1463.

Culick, F. E. C. & Yang, V. 1992 Prediction of the stability of unsteady motions in solid-propellant rocket motors. In *Nonsteady Burning and Combustion Stability of Solid Propellants* (ed. L. De Luca, E. W. Price & M. Summerfield). Progress in Astronautics and Aeronautics, vol. 143, pp. 719–779. *AIAA*.

Fisher, R. A. 1936 The wave of advance of a advantageous gene. *Ann. Eugen.* **7**, 355–369.

Flandro, G. A. 1974 Solid propellant acoustic admittance corrections. *J. Sound Vib.* **36**, 297–312.

Flandro, G. A. 1986 Vortex driving mechanism in oscillatory rocket flows. *J. Propulsion Power* **2**, 206–214.

Flandro, G. A. 1995*a* Effects of vorticity on rocket combustion stability. *J. Propulsion Power* **11**, 607–625.

Flandro, G. A. 1995*b* On flow turning. *AIAA Paper* 95-2730.

Flandro, G. A. & Roach, R. L. 1992 Effects of vorticity production on acoustic waves in a combustion chamber. *Final Tech. Rep. AFOSR* 90-0159.

Hegde, U. G., Chen, T. & Zinn, B. T. 1986 Investigation of the acoustic boundary layer in porous-walled ducts with flow. *AIAA J.* **24**, 1474–1482.

Hegde, U. G. & Zinn, B. T. 1986 The acoustic boundary layer in porous-walled ducts with a reacting flow. In *21st Symp. (Intl.) Combust*., pp. 1993–2000. The Combustion Institute.

Kassoy, D. R., Staab, P. L., Chang, T. Y. & Hegab, A. M. 1997 Co-existing acoustic-rotational disturbances in a coldflow model of a solid rocket motor. *AIAA Paper* 97-0697.

Kirkkopru, K., Kassoy, D. R. & Zhao, Q. 1995 Unsteady vorticity generation and evolution in a model of solid rocket motor: Sidewall mass addition transients. *AIAA Paper* 95-0603.

https://doi.org/10.1017/S0022112000008454 Published online by Cambridge University Press

KIRKKOPRU, K., KASSOY, D. R. & ZHAO, Q. 1996 Unsteady vorticity generation and evolution in a model of a solid rocket motor. *J. Propulsion Power* **12**, 646–654.

KIRKKOPRU, K., KASSOY, D. R., ZHAO, Q. & STAAB, P. L. 1999 Unsteady vorticity field in a long narrow cylinder with sidewall injection. In preparation.

LAGERSTROM, P. A. 1964 In *Theory of Laminar Flows* (ed. F. K. Moore), chap. B, pp. 90–92. Princeton University Press.

MAJDALANI, J. 1998 Characterization of the laminar boundary layer in solid rocket motors. *AIAA Paper* 98-3699.

MAJDALANI, J., FLANDRO, G. A. & ROH, T. S. 1998 Implications of unsteady analystical flow fields on rocket combustion stability. *AIAA Paper* 98-3698.

MAJDALANI, J. & VAN MOORHEM, W. V. 1997 Multiple-scales solution to the acoustic boundary layer in solid rocket motors. *J. Propulsion Power* **13**, 186–193.

MAJDALANI, J. & VAN MOORHEM, W. V. 1998 Improved time-dependent flowfield solution for solid rocket motors. *AIAA J.* **36**, 241–248.

MATTA, L. M. & ZINN, B. T. 1993 Investigation of flow turning loss in a simulated unstable solid propellant rocket motor. *AIAA Paper* 93-0115.

ROH, T. S. & YANG, V. 1995 Transient combustion responses of solid propellants to acoustic disturbances in rocket motors. *AIAA Paper* 95-0602.

SMITH, T. M., ROACH, R. L. & FLANDRO, G. A. 1993 Numerical study of the unsteady flow in a simulated solid rocket motor. *AIAA Paper* 93-0112.

STAAB, P. L. 1998 Three-dimensional acoustic-rotational flows in solid fuel rocket motors. PhD thesis, Department of Applied Mathematics, University of Colorado.

STAAB, P. L. & KASSOY, D. R. 1996 Three-dimensional, unsteady, acoustic-shear flow dynamics in a cylinder with sidewall mass addition. *Phys. Fluids* B **9**, 3753–3763.

STAAB, P. L., ZHAO, Q., KASSOY, D. R. & KIRKKOPRU, K. 1999 Co-existing acoustic-rotational flow in a cylinder with axisymmetric sidewall mass addition. *Phys. Fluids* **11**, 2935–2951.

TAYLOR, G. I. 1956 Fluid flow in regions bounded by porous surfaces. *Proc. R. Soc. Lond.* A **234**, 456–475.

TIEN, J. S. 1972 Oscillatory burning of solid propellants including gas phase time lag. *Combust. Science Tech.* **5**, 47–54.

TSENG, C., TSENG, I. S., CHU, W. & YANG, V. 1994 Interactions between acoustic waves and premixed flames in porous chambers. *AIAA Paper* 94-3328.

VUILLOT, F. 1995 Vortex-shedding phenomena in solid rocket motors. *J. Propulsion Power* **11**, 626–639.

VUILLOT, F. & AVALON, G. 1991 Acoustic boundary layers in solid propellant rocket motors using navier-stokes equations. *J. Propulsion Power* **7**, 231–239.

WILLIAMS, F. A. 1985 *Combustion Theory*. Benjamin/Cummings.

ZHAO, Q. 1994 Nonlinear acoustic processes in solid rocket engines. PhD thesis, University of Colorado at Boulder.

ZHAO, Q. & KASSOY, D. R. 1994 The generation and evolution of unsteady vorticity in a model of a solid rocket engine chamber. *AIAA Paper* 94-0779.

https://doi.org/10.1017/S0022112000008454 Published online by Cambridge University Press